G. Droandi, A. Zanotti, G. Gibertini
Aerodynamic Interaction Between Rotor and Tilting Wing in Hovering Flight Condition
Journal of the American Helicopter Society, Vol. 60, N. 4, 2015, 042011 (20 pages)
doi:10.4050/JAHS.60.042011

Aerodynamic Interaction Between Rotor and Tilting Wing in Hovering Flight Condition

Giovanni Droandi
Post-Doc Fellow
Alex Zanotti
Post-Doc Fellow

Giuseppe Gibertini
Assistant Professor
Dipartimento di Scienze e Tecnologie Aerospaziali,
Politecnico di Milano,
via La Masa 34, Milan, Italy

Abstract

The hovering performance and the lifting capability of tiltrotor aircraft are strongly affected by the aerodynamic interaction between wing and rotors. The tiltwing concept represents an interesting technology to increase the hover performance by reducing the wing–rotor interference. The present work investigates the aerodynamic interaction between wing and rotor in hover for a scaled tiltwing aircraft half–span model. A comprehensive experimental campaign, including force measurements and particle image velocimetry surveys, was performed together with computational fluid dynamics simulations. Numerical predictions were validated using experimental data and were used to describe the flow field.

Nomenclature

A rotor disk area, πR^2

c chord

c_∞ speed of sound

C_P power coefficient, $P/(\rho A \Omega^3 R^3)$

C_T thrust coefficient, $T/(\rho A \Omega^2 R^2)$

$C_{T^\star}$ net thrust coefficient, $T^\star/(\rho A \Omega^2 R^2)$

DL disk loading, T/A

$C_{f,z}M^2$ sectional blade normal force coefficient times Mach number squared, $f_z/(1/2 \rho c_\infty^2 c)$

FM figure of merit, $C_T^{3/2}/(C_P \sqrt{2})$

$FM^\star$ net figure of merit, $C_{T^\star}^{3/2}/(C_P \sqrt{2})$

F aerodynamic force

f sectional aerodynamic force

h vertical distance between the wing rotation axis and the rotor disk

M_{tip} blade tip Mach number

P rotor power

N_b number of blades

Q_{crit} Q criterion, $1/2(\|\mathbf{\Omega}\|^2 - \|\mathbf{S}\|^2)$

R rotor radius

Re_{tip} blade tip Reynolds number

r radial coordinate

$\mathbf{S}$ strain–rate tensor

U velocity component

T rotor thrust

$T^\star$ net thrust, $T - F_z$

x longitudinal coordinate

y spanwise coordinate

z vertical coordinate

τ tilted wing angle

ρ air density

σ rotor solidity, $cN_b/(\pi R)$

θ collective pitch angle

ψ azimuthal angle position

Ω rotational frequency of the rotor

$\boldsymbol{\Omega}$ vorticity tensor

Subscript

x component along x axis

y component along y axis

z component along z axis

Introduction

After about 50 years of research and development, tiltrotor aircraft are reality in the modern rotorcraft scenario, combining the capability to hover and cruise at high speed, like propeller driven aircraft [1]. In general, the tiltrotor concept represents an interesting solution by combining the advantages and the peculiarities of helicopters with modern propeller airplanes, offering a concrete possibility to overcome the main limitations of both worlds [2]. For these reasons and their versatility, tiltrotor aircraft represent a very attractive compromise for the civil aeronautical industry [3, 4]. Nevertheless, the particular layout of this hybrid aircraft concept necessarily leads to a much more complex and demanding design with respect to modern helicopters or propeller airplanes. Even though the tiltrotor concept is so promising, this aircraft is characterized by several intrinsic problems related to different technical areas, i.e. aerodynamics, structures, avionics and flight mechanics.

In helicopter flight mode, one of the most important issues is directly related to the aerodynamic interaction between the wing and the rotors which strongly affects the performance and the lifting capabilities of a tiltrotor aircraft. With the aim of having acceptable hover performance, large rotors were adopted in the actual tiltrotors (XV–15, V–22 Osprey and BA609). Although in hover this solution allows the rotors to provide the necessary amount of lift to overcome the aircraft weight together with the airframe download penalty, aerodynamic interference due to wing–rotor [5] and rotor–rotor [6] interactions remains. The use of large rotors also has other important consequences for tiltrotor aircraft. Indeed, large rotors prevent the take–off and landing in airplane flight mode and lead to important limitations in cruise flight, such as the maximum cruise speed achieved and the operative range, which is limited by a relevant fuel consumption [7].

In particular in the hovering condition, the presence of the wing under the rotor significantly modifies the rotor wake system [8] and changes the rotor performance with respect to the isolated case [9]. In this operating condition, the rotor wake strikes the upper surface of the wing and generates a complex three–dimensional unsteady flow which negatively affects the aircraft performance [10]. As shown by McVeigh [11] and Felker [12], results from hover tests on the 0.658–scaled V–22 half–model demonstrated that the aerodynamic interaction occurring between wing and rotor is responsible for loss of rotor thrust and for wing download. Results found by McCluer and Johnson [13] for the 0.25–scaled Full–Span Tiltrotor Aeroacoustic Model (FS–TRAM) present a similar behavior with respect to previous half–model results, showing that the rotor FM decreases compared to the isolated rotor case [14, 15]. Hover measurements on the FS–TRAM [16] also demonstrated that the rotor downwash impinging on the wing creates a non–negligible download force that is approximately $10\ \%$–$15\ \%$ of the rotor thrust. A small reduction of the wing download in hover can be achieved by rotating the trailing edge flap by a certain angle. As shown by Wood and Peryea [17] and Young et al. [16] on the V–22 half–span and full–span (FS–TRAM) models respectively, a deflection of $65°$–$70°$ may reduce the wing download to a maximum value of about 6–8 $\%$ of the rotor thrust.

Since the improvement of the performance in airplane mode is actually one of the focus points for future developments of new tiltrotor aircrafts, non–conventional tiltrotor configurations have to be further investigated [18, 19] with the aim of preserving the performance in helicopter mode. A possible approach to improve the performance in airplane mode (i.e. the propulsive efficiency and the cruise speed) is to significantly modify the blade shape [20] and reduce the rotor diameter in order to achieve a propeller similar to the airplane propellers [21]. This solution allows sufficient ground clearance for take–off and landing in airplane flight mode, but cannot be directly used in conventional tiltrotor aircraft because such small propellers exhibit higher DL and lower hover efficiency when compared to modern helicopter rotors.

The tiltwing concept is a successful design option which employs small diameter rotors reducing the penalties due to the interactional aerodynamic effects. The main characteristic of a tiltwing aircraft is that the wing pivots together with the small rotors and the nacelles, minimizing the wing surface on which the rotor wake strikes. During the 1950s, the tiltwing concept was first explored by the Vertol Division of Boeing company which designed [22], constructed and tested [23] the VZ–2 (or Model 76) tiltwing research vehicle. Throughout the 1960s, two research programs, the Ling–Temco–Vought (LTV) XC–142 [24] and the Canadair CL–84 [25], were started to investigate the tiltwing principle. Even though the tiltwing aircraft demonstrated good capabilities and high versatility in a wide range of roles, the research programs ended due to a progressive lack of interest by partners. At the beginning of the 2000s, the tiltwing concept was re–introduced by AgustaWestland for the development of the European project ERICA (Enhanced Rotorcraft Innovative Concept Achievement [26]). The main feature of ERICA is the capability to rotate the outer part of the high–mounted wing as well as the rotor–nacelle group that is located at the wing tip. This innovative layout preserves good hover performance [27] and the resulting download force is less than $1\ \%$ of the rotor thrust [28, 29]. However, the ERICA configuration presents some potential drawbacks. For instance, the high DL of the propeller increases the acoustic source noise and tilting the outboard portions of the wing leads to a reduction of the overall wing stiffness. Though the ERICA tiltrotor has been the object of several experimental [30] and numerical [31] studies during the last fourteen years, many aspects of this aircraft configuration require further analysis. A detailed investigation of this promising solution would help engineers during the design process of a tiltwing aircraft. In particular, a correct characterization of the rotor wake geometry together with a description of the flow field between the rotor plane and the tilted wing would be useful to understand the phenomena related to the wing–rotor interaction in this hybrid aircraft, as experimental and numerical databases on tiltwing aircraft are very few and not public.

In the last few years, many investigations were carried out on the wing–rotor interaction problem for conventional tiltrotor configurations. For instance, Chiaramonte et al. [32] analyzed different flow configurations to simulate different conditions in the whole flight envelope using a propeller/nacelle/half–wing model. Darabi et al. [8] gave descriptions of the mean and time–dependent rotor wake flow over a XV–15 tiltrotor model in hover using stereoscopic Particle Image Velocimetry (PIV), while Grife et al. [33] proposed the use of active flow control to reduce hover download on a scaled V–22 model. Examples of computational studies about tiltrotor aircraft in hover are the works by Meakin [34], Potsdam and Strawn [10] and Wissink et. al. [35], where complex hover configurations were predicted using different implementations of the Navier–Stokes equations.

In this framework, a research activity was started at the Department of Aerospace Science and Technology (DAER) of Politecnico di Milano to study the aerodynamic interference between the wing and rotor on a high–performance tiltwing aircraft. A reference geometry of a tiltwing aircraft in the same class of ERICA was defined by means of a statistical approach [36]. In particular, a linear regression technique (using the number of passengers as the independent variable) was applied to the main features (i.e. wing and fuselage dimensions, rotor radius, number of rotor blades and aircraft weights) of established tiltrotor aircraft configurations in order to define the geometry [37, 38]. Preliminary numerical calculations were used to get an initial insight on the problem. A $1/4$–scaled wind tunnel half–span model [28] was designed in order to investigate the hovering flight condition. The aim of the present work is to describe the comprehensive experimental campaign carried out on the tiltwing half–span model and the numerical activity performed on the same geometry for the same operating conditions. The results of both experimental and computational activities are used to provide a detailed insight about the aerodynamic interaction between the rotor and wing in hover. In particular, both the aircraft performance and rotor wake geometry were investigated by means of forces measurements and PIV surveys carried out in the open test section of the Politecnico di Milano Large Wind Tunnel (GVPM). High–fidelity Computational Fluid Dynamics (CFD) calculations were used to help the description of the flow field about the rotor/wing system and to better understand wind tunnel data. The computations were performed with the code ROSITA (ROtorcraft Software ITAly) developed at DAER, which is a Reynolds Averaged Navier–Stokes (RANS) equations solver coupled with the one–equation turbulence model of Spalart–Allmaras.

Experimental set up

A tiltwing aircraft in the same class of ERICA was considered for the present study. The reference aircraft was assumed to be a civil passenger transportation aircraft with a capacity of 22 people plus baggage. The reference full–scale aircraft geometrical dimensions and characteristics are reported in Table 1 (for further details on the full–scale aircraft see Droandi [29]).

A new experimental test rig [28] was designed and manufactured in the DAER Aerodynamics Laboratory to study the aerodynamic interaction between wing and rotor in a tiltwing aircraft in hover. The test rig allows to investigate the sensitivity of the aircraft performance to different parameters, as for instance the wing configuration and the vertical distance between the wing and the rotor disk.

Tiltwing half–model

The experimental half–span model was $1/4$–scale with respect to the full–scale aircraft (see Table 1). The test rig consisted of two main components: the rotor system and the half–wing with an image plane. The two main systems were supported by two independent supporting structures and allowing the independent measurements of the rotor and the wing loads. The experimental rig also enabled tests of the isolated rotor. Figure 1 shows the whole test rig as well as the Cartesian x–y–z model reference system. The origin of the reference system was located on the rotor hub, at the intersection point between the rotor shaft axis (corresponding to the upward z–axis) and the rotor disk. The y–axis was parallel to the wing tilting axis, pointing starboard. Using the right–hand rule, the x–axis was defined accordingly.

The four–bladed rotor had a radius of $R = 0.925\ m$. The design of the aerodynamic blade shape was generated using a multi–objective optimization procedure adopted in the frame of genetic optimization techniques. A detailed description of the shape optimization procedure is given in the work of Droandi and Gibertini [39] where a detailed characterization of the blade geometry is also presented. The thrust requirements for the rotor design were defined on the basis of estimated values of the aircraft weight and drag obtained by means of classical preliminary design approach [36].

The collective, longitudinal and lateral pitch controls were provided to the blades by means of three independent electric actuators acting on the swashplate. Each electric actuator was equipped with a linear potentiometer providing the feedback signal on the actual position of each command. The rotor hub was fully articulated and was equipped with flap and lead–lag hinges and a pitch bearing. Each blade hinge was instrumented with a high–accuracy Hall–effect sensor to measure the pitch, lead–lag and flap angles directly.

The rotor rotated in anti–clockwise direction and was powered by an hydraulic motor (maximum power of $16\ kW$ at $3000\ rpm$) located inside a swiveling base positioned on an aluminum base. The rotor hub was mounted on a rigid pylon containing the shaft and fixed on the swiveling base. A 24–channel slip ring was used for the transmission of electrical power and measurement signals to and from the rotating part of the rotor hub. A Hall–effect sensor was employed to measure the rotational speed of the rotor and to trigger the PIV image acquisition with a prescribed azimuthal position (ψ) of a given blade. In this regard, a selected blade (master blade) was considered in the azimuthal reference position ($\psi = 0°$) when the blade was over the wing with the $25\ \%$ chord axis of the blade root airfoil parallel to the wing tilting axis. A six–component strain gauge hollow balance was embedded in the upper part of the pylon under the rotor hub. A hollow shaft, passing through the balance, was instrumented with strain gauges to measure the rotor torque. The instrumented shaft was joined to the transmission shaft by a torsionally stiff steel laminae coupling. The complete system was checked by means of reference weights and a maximum error of $0.5\ N$ was found. The nacelle, manufactured in carbon fiber, had an external maximum diameter of $0.27\ R$. The airloads acting on the nacelle were not measured. The air intake was not reproduced on the nacelle model.

The half–wing model length was $1.90\ R$ and comprised two parts: a fixed inner part, with $1.01\ R$ span, and an outer part that could rotate around the axis at $25\ \%$ of the local chord from $\tau = 0°$ (untilted configuration, airplane mode) to $\tau = 90°$ (tilted configuration, helicopter mode), as illustrated in Fig. 2. The wing was linearly tapered, untwisted and with NACA 64A221 airfoil [40,41]. The chord was $0.81\ R$ at the wing root and $0.56\ R$ at the tip. The root section of the wing intersected the aircraft symmetry plane. The internal structure of both wing parts was made of extruded polystyrene foam with aluminum ribs at the extremities. The external skin of the wing was made by 2–layers of carbon fiber skin. The wing was mounted on an independent vertical traversing system to change the vertical distance h between the wing rotation axis and the rotor disk. Forces and moments on the wing were measured by a seven–component strain gauge balance located at the wing root. A square image plane with $2.2\ R$–side was positioned at the fixed wing root to reproduce the symmetry plane [11, 42, 43]. The image plane was fixed on the support of the wing traversing system, the upper edge was positioned at a height of $0.9\ R$ over the rotor disk. At the longitudinal plane of symmetry of a conventional tiltrotor aircraft (in which the half–wing span is on the order of the rotor radius) the effects of rotor/rotor and wing/rotor interactions generate a highly turbulent fountain flow which affects the rotor performance. As shown by Polak et al. [6], the use of an image plane with a half–span model is not correct for conventional tiltrotors because the mean velocity and the turbulent kinetic energy are assumed to be zero on that plane. With an image plane, the velocity field in the fountain region is significantly modified [10], a high–velocity wall jet is created on the image plane and more turbulent kinetic energy is ingested by the rotor. As illustrated by Darabi et al. [8], another consequence of using an image plane is the non–negligible displacement of the vortex wake boundaries with respect to the full–span case. However, the comparisons of experimental works on semi–span models by McVeigh [11], Farrell [42] and Felker [12] with XV–15 and V–22 flight tests and full–span model tests by McCluer and Johnson [13] and Young et al. [16] demonstrated that the image plane approximation of a full–span hovering tiltrotor is justified for the evaluation of the overall rotor performance and wing download, even though the flow structure is not correct as shown by Darabi et al. [8] and by Potsdam and Strawn [10]. The use of an image plane is justified for a hovering tiltwing aircraft and has already been used in the TILTAERO (TILTrotor interactional AEROdynamics, [31]) and ADYN (Tiltrotor Acoustic DYnamic and Noise, [44]) projects. Indeed, the rotor/rotor interaction is reduced since the rotor radius is small compared to the half–wing span (which is twice the rotor radius in the present case). Moreover, even though the downwash velocity is higher than in a conventional tiltrotor because of the higher rotor DL, the wing blockage effect is strongly reduced once the outboard wing portion is rotated ($\tau = 90°$). Nevertheless, the presence of the image plane will affect the flow in the untilted wing configuration ($\tau = 0°$). Therefore, the results obtained for the untilted wing configuration were used for a qualitative analysis of the airloads behavior of a classical tiltrotor configuration compared to a tiltwing configuration.

To ensure that measurements were free from wall and wake recirculation effects, the half–span tiltwing model was located in the center of the open test section of the Politecnico di Milano GVPM and hover tests were carried out in the large plenum chamber surrounding the test section, as shown in Fig. 3. The test rig set up was largely used for isolated rotor tests [45]. The rotor disk was positioned at a height of $5\ R$ from the ground and its wake could freely travel along the plenum floor for a minimum of $11.3\ R$. The ceiling was $7.6\ R$ above the rotor and the nearest wall was $11.3\ R$ from the model center. Even though some recirculation was present, the distance of the walls, the floor and the ceiling from the rotor disk were similar as in the experiment described by Polak et al. [6].

Rotor operating conditions

During the experiment, the nominal rotational speed of the rotor was kept constant at $1120\ rpm$. The tip Mach number was $M_{tip} = 0.32$ which corresponds to half the tip Mach number of the full–scale aircraft at design point in hover [39]. The range of C_T/σ values during the tests varied from 0.001 to 0.093 and were achieved by controlling the collective pitch of the rotor head. Although the declared maximum power of the hydraulic pump which drove the motor was $16\ kW$, the power given by the motor was limited by the engine capacity. Therefore, the maximum power achieved during all the tests was about $8.5\ kW$ corresponding to a maximum collective pitch of $\theta = 13.4°$. Some differences with respect to the full–scale aircraft are, in principle, expected due to Mach number effects as well as to Reynolds number effects but several previous works (for example [6,8,11,33]) suggest that the behavior of the rotor wake flow is essentially the same at smaller scale. Although the M_{tip} and Re_{tip} numbers on the model (respectively 0.32 and 9.87×10^5) were lower with respect to the full–scale aircraft (respectively 0.64 and 7.89×10^6) these differences were on the order of those discussed by Polak and George [46] and were not expected to influence the test results significantly. Furthermore, the ratio between the aerodynamic forces acting on the wing and the rotor thrust should be independent of the M_{tip} because there were no relevant Reynolds number effects on the wing, as discussed by McVeigh [11]. In fact, since the Reynolds number based on the aircraft mean wing chord and the slipstream axial velocity ($2\Omega R\sqrt{C_T/2}$) was 8.60×10^5 for the scaled model and 6.84×10^6 for the full–scale aircraft, this difference was not expected to significantly affect the force measurements on the wing.

PIV set up

The flow structures related to the aerodynamic interaction between the rotor wake and the wing were investigated by means of 2D PIV surveys carried out for both the isolated rotor and the half–model with the tilted wing ($\tau = 90°$) for the same rotor trim condition ($\theta = 12°$). The employed PIV instrumentation [47] was composed of a Nd:YAG double–pulsed laser with 200 mJ output energy and a wavelength of 532 nm and a double–shutter CCD camera with a 12 bit, 1952 $\times$ 1112 pixel array. A schematic of the PIV set up is shown in Fig. 1. The camera was mounted on a single–axis traversing system to move the measurement window vertically. The laser was alternatively mounted below the rotor disk to light a plane at constant x and in front of the tilted wing to light different planes along the wing span at constant y. In particular, an azimuthal measurement plane perpendicular to the rotor disk at $x/R = 0$ was considered for the isolated rotor tests (see the blue x–constant plane of Fig. 4). Since the previous measurement plane contained the wing tilting axis, the measurement plane was shifted at $x/R = -0.079$ when the wing was present (half–span model) in order to avoid the interference of the light sheet with the tilted wing (see the red x–constant plane of Fig. 4). The PIV measurement area for the isolated rotor was $0.38\ R$ wide and $0.90\ R$ high while for the half–span model configurations the measurement area on the x–constant plane was $0.38\ R$ wide and $0.63\ R$ high. In order to achieve better resolution of the image pairs, the measurement area was composed, respectively, by four (isolated rotor) and three (half–span model) adjacent windows with a small overlapping band between them. The spanwise position of the outer edge of the measurement area corresponded to the wing tilting section while the upper edge was located at $z/R = 0.15$.

Furthermore, y–constant planes at $y/R = -0.69$ and $y/R = -0.79$ were surveyed to evaluate the swirl in the rotor wake flow over the leading edge of the tilted wing. For this test case, the PIV measurement area was $0.27\ R$ wide and $0.30\ R$ high, and was composed by three adjacent windows with a small overlapping band between them (see the green y–constant planes of Fig. 4).

Phase–locked PIV measurements were carried out by synchronizing the laser pulses with a prescribed azimuthal position of the rotor master blade. In particular, PIV measurements were carried out from $\psi = 15°$ to $\psi = 90°$ with a $15°$ step. The synchronization of the PIV instrumentation was controlled by a 6–channel Quantum Composer QC9618 pulse generator. A particle generator with Laskin atomizer nozzles was used for the seeding. The image pairs post–processing was carried out using the PIVview 2C software [48] developed by PIVTEC. Multigrid interrogation method [49] was employed to correlate the image pairs, starting from a 96 pixel × 96 pixel to a 32 pixel × 32 pixel interrogation window. In order to investigate the spatial evolution of the blade tip vortices, the vector field on the x–constant measurement planes was computed by averaging 100 vector fields for each considered azimuthal position of the master blade (phase–average). On the other hand, the vector field on the y–constant planes will be presented as the global–averaged field, obtained as the mean of all the phase–averaged computed vector fields.

Numerical calculations

A numerical activity was carried out in parallel to the experimental tests in order to get more information about the physics of the phenomena related to the aerodynamic interaction between the wing and the rotor wake.

Flow solver ROSITA

The CFD code ROSITA (ROtorcraft Software ITAly) [50] numerically integrates the unsteady Reynolds Averaged Navier–Stokes (RANS) equations, coupled with the one–equation turbulence model of Spalart–Allmaras [51]. Multiple moving multi–block grids can be used to form an overset grid system by means of the Chimera technique, as described next. To simplify the solution of the flow field in overset grid systems, the Navier–Stokes equations are formulated in terms of the absolute velocity, expressed in a relative frame of reference linked to each component grid. The equations are discretized in space by means of a cell–centered finite–volume implementation of the Roe's scheme [52]. Second–order accuracy is obtained through the use of MUSCL extrapolation supplemented with a modified version of the Van Albada limiter introduced by Venkatakrishnan [53]. The viscous terms are computed by the application of the Gauss theorem and using a cell–centered discretization scheme. Time advancement is carried out with a dual–time formulation [54], employing a 2^{nd} order backward differentiation formula to approximate the time derivative and a fully unfactored implicit scheme in pseudo–time. The equation for the state vector in pseudo–time is non–linear and is solved by sub–iterations [55]. In the dual–time method, there is no stability limit with respect to the size of the physical time step Δt and this approach can lead to a large reduction in CPU time compared to a fully implicit method in physical time. The physical time step Δt is here only limited by solution accuracy requirements. However, there is a stability condition on the pseudo–time step, as shown by Hirsch [56] for viscous flow calculations. The generalized conjugate gradient (GCG), with preconditioning based on a block incomplete lower–upper factorization, is used to solve the resulting linear system.

The connectivity between the (possibly moving) component grids is computed by means of the Chimera technique. The approach adopted in ROSITA is derived from that originally proposed by Chesshire and Henshaw [57], with modifications to further improve robustness and performance. The domain boundaries with solid wall conditions are firstly identified and all points in overlapping grids that fall close to these boundaries are marked as holes (seed points). Then, an iterative algorithm identifies the donor and fringe points and lets the hole points grow from the seeds until they entirely fill the regions outside the computational domain. To speed up the search of donor points, oct-tree and alternating digital tree (ADT) data structures are employed.

The ROSITA solver is fully capable of running in parallel on computing clusters. The parallel algorithm is based on the message passing programming paradigm and the parallelization strategy consists in distributing the grid blocks among the available processors. Each grid block can be automatically subdivided into smaller blocks by the solver to attain an optimal load balancing.

Numerical models

Numerical calculations with the CFD code ROSITA were computed following two different approaches with increasing complexity to model the rotor. The numerical activity considered the hover condition with the external wing completely tilted ($\tau = 90°$). A steady–state approach was used in order to get information about the mean aerodynamic loads acting on the wing. This approach validated the reliability of both the grids and the simulation results by comparison with wing force measurements. An actuator disk model was used to represent the rotor loads instead of simulating the flow around rotating blades. Since the steady–state assumption gives a strong reduction of computational times with respect to the unsteady approach, steady calculations were used to numerically evaluate the mean effects of the rotor wake on the wing at several C_T/σ corresponding to different test conditions, as reported in Table 2. Moreover, a time–accurate approach was employed to investigate both the rotor and wing loads variation in time. The unsteady computational results allowed analysis of the phenomena related to the unsteady nature of the rotor/wing aerodynamic interaction. In this case, this approach was used only for the trim condition TC6 of the rotor (the same used for the PIV surveys) due to the very high computational effort required. For the same reason, a proper grid convergence study was not carried out in the present work. However, a grid dependence study was performed for the isolated rotor case described in Droandi [29].

Cartesian multi–block grids were used to represent the flow field around bodies and the Chimera method was employed to exchange the solution between different grids. Using the Chimera method, a set of grids was built and used to run alternatively steady and unsteady simulations by only replacing the actuator disk grid with four equal grids describing the rotating blades. With the aim of limiting the total number of cells, the background mesh was composed of 2 different Cartesian multi–block grids, one fine (the inner grid, Far–field 1) and one coarse (the outer grid, Far–field 2). All the other grids were contained inside the finer background grid, having similar spatial resolution at the outer edges, as shown in Fig. 5(a). Both wings were meshed with a C–H topology while the nacelle was meshed with an O topology. In general, the body grids had high density close to the body surfaces and limited spatial extension around them. All the aforementioned grids were created with ANSYS ICEMCFD. To guarantee a sufficient overlap region for the Chimera tagging procedure, a very small gap (on the order of $0.001\ R$) between the two wings and between the outer wing and the nacelle was introduced. A magnified view of the gap region between the tilted wing and the nacelle is shown in Fig. 5(b). The outer boundaries of the wing grids were at $0.2\ R$ from the wing surfaces except at the trailing edge region where the grid was extended up to $1.4\ R$ from the edge. The outer boundary of the nacelle grid was located at $0.2\ R$ from the surface in all directions. The nacelle grid and the outer wing grid were contained inside an intermediate cylindrical grid (with a radius of $1.3\ R$) which was used to better capture the rotor wake of the actuator disk or of the rotating blades. The parameters of the grids are reported in Table 3. A symmetry boundary condition was applied to the wing symmetry plane, while a no–slip boundary condition was applied on both wings and nacelle surfaces. Far–field boundary conditions were imposed at the remaining domain boundaries.

In the steady–state approach, simulations were carried out by reproducing the effects of the rotor with an actuator disk. The actuator disk model embedded in ROSITA approximates the forces applied by the rotor blades to the air flow over a disk having the same diameter as the rotor. The actuator disk grid had zero thickness in a single layer of cells of a cylindrical O–H grid. A non–uniform source load distribution was specified to reproduce the desired force (per unit area) distribution [58]. Since the load distributions on the rotor disk were imposed a priori, any effect of the flow distortion on the rotor loads due to the wing presence was not included for the present formulation of the actuator disk model. A view of the grid system for the steady computations is shown in Fig. 6(a). The disk without thickness was coincident with the tip path plane of the rotor. Since this plane was defined by the rotor trim condition, the spatial location of the disk changed for every C_T/σ analyzed in order to reproduce the actual coning angle that depended on the blade flapping. Each force distribution on the disk was derived from a single–blade steady calculation of the isolated hovering rotor, as described by Droandi [29].

As previously mentioned, the computational mesh for the unsteady simulation was obtained by replacing the actuator disk grid with four identical grids, each one composed by 1.813×10^6 cells and containing one blade. A C–O grid meshing topology was used to ensure a good node distribution and orthogonality in the proximity of the blade surface. A view of the grid system used for the unsteady simulation is shown in Fig. 6(b). The blade was discretized using a hyperbolic law along the chord–wise, spanwise and normal surface directions. The outer boundaries of the grid were at 0.9 R from the blade surfaces except in the spanwise direction where they were at 0.5 R from the blade tip and in the chord–wise direction where boundaries were at 1.2 R from the trailing edge.

Since in hovering flight some regions of the flow field around the aircraft are characterized by very low velocities, both steady and unsteady computations were carried out using the Turkel's low Mach number preconditioner [59]. Low values of the Courant–Friedrichs–Lewy (CFL) number were employed in all calculations. Each steady simulation took about 21–25 hours with a CFL equal to 5 by running the CFD solver in parallel on 64 processors until convergence was reached. The time–accurate simulation required about 44 days to complete 10 rotor revolutions, with each revolution requiring about 98 hours. The solution was achieved by running the ROSITA code in parallel on 128 processors with a CFL of 2.5.

Results and discussion

The experimental activity began with characterizing the performance of the isolated rotor. Then, the rotor–wing aerodynamic interaction was investigated by considering two wing configurations (tilted and untilted) at two vertical distances of the wing with respect to the rotor disk.

Analysis of airloads

Figure 7(a) shows the behavior of the isolated rotor FM as function of C_T/σ, while the measured power coefficient C_P behavior is shown in Fig. 7(b) as function of C_T. The maximum values of the standard deviation of the thrust and power coefficients were respectively equal to 1.08×10^{-4}, 1.35×10^{-5} while the maximum value of the standard deviation for the rotor FM was 2.75×10^{-3}. The standard deviation was evaluated on the basis of 40 measurements acquired for the trim condition at $\theta = 12°$ (each measurement was the mean value over 5 s acquisition time). The maximum value of FM achieved during the isolated rotor tests was 0.71 (at $C_T = 0.0178$ and for $C_P = 0.0023$). However, the maximum value of C_T measured during experiments was 0.0180 because a further increase of collective pitch angle lead to a power limit of the motor capability. This value is slightly lower than the thrust coefficient $C_T = 0.0215$ considered for the hovering condition in the design of the blade shape [39].

After the isolated rotor tests, the wing was installed in the test rig. Untilted ($\tau = 0°$) and tilted ($\tau = 90°$) wing configurations were tested to investigate how the airframe affects the aircraft performance in hover. The vertical force lifting the aircraft is given by the sum of the effective rotor thrust (T, measured by the rotor balance) and the wing vertical load (F_z, measured by the wing balance). The resulting net thrust force ($T^{\star} = T - F_z$) has to be considered to evaluate the real efficiency of the system. For this reason, in both Fig. 7(a) and 7(b), the performance relative to the half–span model, the figure of merit and the thrust coefficient, are reported in terms of net thrust $T^{\star}$. When the wing is untilted, the net $FM^{\star}$, the net $C_{T^{\star}}$ and the rotor C_P are strongly influenced by the presence of the wing. In this case, the power required to hover is much more than in the isolated rotor case and the maximum measured C_P increment was about 26 $\%$ for both the lower and upper wing positions analyzed. This feature is due to the download produced by the rotor wake on the wing ($h/R = 0.465$), resulting on the order of 16 $\%$ of the rotor thrust T, as shown in Fig. 8(a) where the ratio between the vertical wing load F_z and the rotor thrust T is given as function of rotor C_T/σ. Although the untilted wing gave a partial ground effect increasing the rotor thrust [11], the vertical wing load F_z was higher than the rotor thrust increment, decreasing the half–span model net thrust $T^\star$ with respect to the isolated rotor case. Notice that the wing download ratio F_z/T decreased as the rotor thrust increased. At very low pitch angles, the outboard part of the blade is not contributing to the rotor thrust due to the blade twist angle distribution. Thus, at low C_T/σ (low rotor pitch angles) the ratio between the wing area affected by the rotor wake and the effective part of the rotor disk is higher than at high C_T/σ values where the entire blade is loaded. The measured trend of the wing download ratio for the untilted configuration is consistent with the results found by Young et al. [16] for the V–22 full–span model, although in that case the wing download ratio ($10\ \%$) was slightly lower compared to present results. The ratio of the wing area affected by the rotor wake and the rotor disk area is smaller for the V–22 aircraft, which explains the lower download compared to the tiltwing model.

On the other hand, the performance for the tilted wing configuration shows a very different behavior compared to the untilted case since the aircraft performance was far less affected by the wing presence. The experimental results exhibit a remarkable decrease of the power required due to the drastic reduction of the vertical load F_z acting on the wing. In particular, as shown in Fig. 8(a), the vertical force/thrust ratio is found to be less than $1\ \%$ for all the C_T/σ tested and for C_T/σ greater than 0.058 it is slightly positive (upload). The maximum value of the standard deviation of the vertical wing force/thrust ratio was equal to 4×10^{-4}. By reducing the wing incidence with respect to the wake flow (i.e. by rotating the outer portion of the wing), the wing behaves as an aerodynamic body instead of a bluff body. For the tilted configuration, the outer part of the wing was set with the airfoil chord aligned vertically with the z–axis. Therefore, a non–zero lift force normal to the relative local velocity can be expected due to the airfoil camber. The incidence induced by the rotor wake swirl further increased the local incidence and created a small upward lift component. In conclusion, in the tilted configuration the rotor performance is very similar to the performance of the isolated rotor in hover (Fig. 7(a)).

For the tilted configuration, the measured longitudinal force acting on the wing was higher than the vertical component and always positive, as shown in Fig. 8(b). In this case, the maximum value of the standard deviation of F_x/T was equal to 2×10^{-2} and was determined as described for F_z/T. In particular, for $C_T/\sigma > 0.02$, F_x/T for the tilted wing configuration is nearly constant (about 4.5 %). In the untilted configuration, F_x is almost zero. The measurement of non–negligible longitudinal force component acting on the wing in the tilted configuration demonstrates that, for the present hovering tests, the tiltwing model is not in a trimmed condition. The results are relative to the tilted wing configuration ($\tau = 90°$), that was assumed as a reference condition. In fact, the presence of non–negligible longitudinal force component acting on the wing negatively influences hovering flight but may also affect the conversion phase of the aircraft. Therefore, one of the goals to be considered during the design process of a tiltwing aircraft is to avoid the residual longitudinal force on the wing.

For both of the tilt wing angles considered, the tests were carried out with the wing alternatively positioned with its rotation axis at a vertical distance from the rotor disk of $h/R = 0.465$, which corresponded to the design wing–rotor distance (see Table 1), and $h/R = 0.681$. Experimental data suggested that the aircraft performance was almost independent of the wing position, as shown in Fig. 7(a) and 7(b). Indeed, in the tilted configuration the rotor wake impinged on a small portion of the wing surface which was not sufficient to affect the rotor loads, while, in the untilted case, although the rotor wake covered the whole wing surface, the difference between the upper and lower wing positions did not significantly affect the rotor performance. Tests results also revealed that wing loads were not affected by the wing/rotor distance, except for the wing vertical load F_z in the untilted configuration, as shown in Fig. 8(a) and 8(b). In the latter case, F_z/T decreased about 6 % when the wing was moved down since the induced velocity in the rotor slipstream slightly decreased as the distance from the rotor disk increased.

Steady calculations were carried out on the hovering aircraft with the tilted wing ($\tau = 90°$) and placed at a distance of $h/R = 0.465$ from the rotor disk. The experimental test conditions were simulated and several load distributions corresponding to different C_T/σ were imposed on the actuator disk (see Table 2).The predicted mean aerodynamic loads acting on the wing are compared with experimental data in Fig. 8. The agreement between numerical calculations and measured F_x/T and F_z/T is rather good in both cases, demonstrating the reliability of the grids employed in the simulations and the capability of the CFD code ROSITA to properly predict the global loads on the wing. However, for C_T/σ higher than 0.06, the values of the vertical force component F_z predicted by the CFD code are slightly lower with respect to the experimental data. An upload effect is still present but the predicted force/thrust ratio is less than about 0.5 %. Both the values (about 4.5 % for $C_T/\sigma > 0.02$) and the trend of the longitudinal force component F_x predicted with ROSITA agree with test results.

The time–accurate simulation was carried out for the trim condition TC6 of the rotor ($\theta = 12°$, $\beta = 2.5°$) for a total of 10 rotor revolutions for the tilted wing configuration ($\tau = 90°$). At every time step the blades and their grids were rotated by $2°$. To start the unsteady simulation, an impulsive start was used at the first time step and the rotor forces became nearly periodic after the fourth revolution, as shown in Fig. 9(a) and 9(b) where the rotor thrust and power time history are shown respectively. For hover, the rotor wake system needed more than four revolutions to reach a fully developed state. After 6 rotor revolutions the wing was fully immersed in the rotor wake and also the wing forces became nearly periodic. After 8 revolutions the rotor wake was convected sufficiently far downstream from the wing system and both the rotor and the wing loads reached a converged state, demonstrating however a dependence on the blade azimuthal position. Figure 10(a) illustrates the behavior of the global wing vertical F_z and longitudinal F_x loads during the 10 revolutions. In particular, the time history of the contributions given by each single portion of the wing to the vertical and longitudinal loads in the last revolution are shown in Fig. 10(b). The predicted behavior of the airloads on the wing surfaces exhibited the characteristic frequency of 4 cycles per revolution, typical of a four–bladed rotor. As expected, this phenomenon is evident for the outer wing portion which is completely immersed in the rotor wake flow. Nevertheless, small oscillations exhibited by the inner wing loads demonstrated that there is a small effect of the rotor wake system also over the inboard portion of the wing even for high C_T/σ. The wing global loads predicted by the unsteady calculation, averaged over the last rotor revolution, are shown as function of C_T/σ in Fig. 8 together with experimental data and steady calculations. As shown in these figures, wing loads are well predicted by the time accurate CFD simulation. In particular, for the vertical force F_z the agreement between the unsteady result and the experimental data is rather good and slightly better than in the steady case.

The aircraft hover performance are shown in Fig. 7(a) and 7(b), detailing respectively the FM as function of C_T/σ and C_P against C_T. A rather good agreement with experimental data was also found for the rotor loads. Indeed, the rotor thrust and power are just slightly over–predicted by ROSITA (the predicted C_P resulted 5.5×10^{-5} higher than the experimental data at the same C_T).

The load distribution along the blade span at four different azimuthal positions is presented in Fig. 11

for $\tau = 90°$. A reduction of the blade outboard loading at $\psi = 0°$ (over the wing) is apparent and is only partially compensated by a load increase on the third quarter of the blade. The resulting thrust loss is however much lower than in a tiltrotor with conventional configuration [10] and marginally affects the overall tiltwing aircraft performance. This behavior is the result of a different induced velocity distribution due to a different relative positioning of the wake vortices. This behavior is confirmed by the vorticity magnitude contours illustrated in Fig. 12 showing two different flow regions around the rotor (inner and outer side, see Fig. 12(a)) extracted when the master blade was located at $\psi = 0°$. For an isolated rotor, the blade tip vortex moves towards the rotor axis, due to the wake contraction, inducing an upwash velocity at the blade tip. In the present case, the wake contraction is locally reduced over the wing so that the vortex moves down more vertically. Indeed, the tip vortex issued by the preceding blade assumes two different positions (with respect to the blade tip) for the outer and for the inner side (see respectively Fig. 12(b) and 12(c)). As a consequence, the upwash on the blade tip is smaller on the inner side producing the observed decrease of the loading on the blade tip region. The vortex center, identified by the vorticity peak, is located respectively at $r/R = 0.905$ and at $z/R = -0.007$ for the inner side and at $r/R = 0.900$ and at $z/R = 0.011$ for the outer side.

Flow field analysis

In hover, the interaction between the rotor blade tip vortices and the tilted wing is responsible for the growth of unsteady phenomena that could negatively affect the aircraft structure and dynamics. Force measurements and CFD calculations revealed that rotor and wing airloads are characterized by a periodic behavior which depends on the azimuthal position of the rotor blades with respect to the wing. In order to better describe how the wing modifies the rotor wake geometry, PIV surveys were carried out both for the isolated rotor and for the half–span model with the tilting wing set at $\tau = 90°$. Two different wing–rotor distances ($h/R = 0.465$, $h/R = 0.681$) were considered. During PIV surveys only one rotor trim condition was analyzed. The collective blade pitch angle was $\theta = 12°$ and the rotor rotational speed was equal to $1120\,rpm$.

Figure 13 shows the vorticity contours for the isolated rotor. The measurement plane was fixed

(x =constant, see Fig. 4) and data were acquired for a blade phase–locked range of $15^\circ \leq \psi \leq 90^\circ$. The vorticity fields of the different blade phases clearly show the progressive rotor wake contraction. Figure 13(a) shows the newly generated tip vortex. With respect to this vortex, the one released by the preceding blade is located sensibly closer to the rotor shaft but just slightly displaced in the vertical direction.

The spatial evolution of the tip vortex core location was analyzed by identifying the approximate vortex center with the position of the maximum vorticity. The evolution of the isolated rotor wake boundary is shown in Fig. 14 showing the tip vortex core displacements at the different blade azimuthal positions on $r - z$ plane. The radial position of the tip vortex core is constant after $z/R = -0.4$, thus the maximum contraction of the rotor wake assumes a radius of about $0.78\ R$. However, around $z/R = -0.5$ the wake boundary shows a local contraction that is apparent from $\psi = 30^\circ$ to $\psi = 75^\circ$. This ”kink” in the wake boundary profile is due to the instability of the wake helical structure. Indeed, this structure is characterized by an instability [60] that is basically the same instability of a 2D vortex array [61] producing the well–known phenomenon of vortex pairing. The vortex pairing is clearly visible in Fig. 13 with the consequent production of the kink in the vortex–cores connecting lines of Fig. 14. The same behavior was observed from the PIV measurements by Darabi et al. [8] in the wake of the XV–15 rotor as well as from the shadowgraph flow visualization by Swanson and Light [43].

The phenomena observed for the isolated rotor case is next compared with the results obtained when the wing is introduced in the test rig. The PIV azimuthal surveys carried out for the isolated rotor are directly compared with the PIV surveys on the x–constant window of the half–span model; however, as the measurement window does not strictly lie on an azimuthal plane, an equivalent phase shift of about 5° is produced with respect to the isolated rotor results.

For the upper wing position case (Fig. 15(a), 15(c) and 15(e)), the presence of the wing prevents the natural wake contraction so that the minimum wake radius is larger than for the isolated rotor case.

For the lower wing position case (Fig. 15(b), 15(d) and 15(f)), the wake boundary traced by the vortex cores is monotonically contracting until the wing leading edge position where a wake enlargement is observed forced by the wing interference.

In order to measure the unsteadiness of the vortex position, the standard deviation of the vortex core center position was computed. Figure 16 shows that, for the blade azimuthal position $\psi = 60°$, the vortex wandering [62] is almost negligible near the rotor plane. Close to the wing, the vortex diffusion observed in Fig. 15, is mainly due to the vortex core position unsteadiness as indicated in Fig. 16.

Figures 17(a) and 17(b) show the rotor tip vortex spatial evolution, as resulted from the unsteady CFD simulation, by means of the visualization of the Q criteria wake iso–surfaces respectively for $\psi = 30°$ and $\psi = 60°$. The vorticity contours measured in the x–constant plane for the same conditions are also presented. The numerical prediction of the tip vortex core positions during the rotor revolution are in good agreement with the data, confirming the reliability of the simulation. Further considerations about the flow field behavior between the rotor disk and the wing can be deduced from the unsteady CFD calculation results. In particular, Fig. 18 illustrates the vorticity magnitude iso–surfaces for one azimuthal blade position ($\psi = 60°$). This representation shows that when the three–dimensional vortex structure reaches the tilted wing leading edge region, the structure is broken in two parts that are convected downstream. Around the wing's leading edge, the vorticity is strongly diffused, locally destroying the coherence of the vortex structure.

A comparison of the rotor wake boundary for the different tested configurations is presented in Fig. 19. The vortex core positions were plotted for all phase–locked positions. The upper region of the rotor wake assumes the same shape for all three configurations. The wake obtained with the wing in the lower position ($h/R = 0.681$) has a profile similar to the isolated rotor case except for the region just above the wing. In fact, in this flow area the isolated rotor wake exhibits the previously described kink while for the case of the lower wing position, the wake expansion due to the wing is apparent. For the upper wing position case ($h/R = 0.465$), the maximum contraction of the rotor wake is observed at $z/R = -0.14$ with a radius of about $0.85\ R$, thus sensibly larger than the value of about $0.8\ R$ obtained for the $h/R = 0.681$ case. The vortex core trajectory computed by the unsteady CFD simulation for the upper wing configuration is in fairly good agreement with the experiments. A wake boundary contraction of the same order was also observed in the experiments by Darabi et al. [8] and by Swanson and Light [43] carried out on conventional tiltrotor configurations.

Figure 20 shows the distribution of the vertical velocity component U_z at several vertical positions below the rotor for the azimuthal blade angle $\psi = 15°$. In the isolated rotor case, for the inner part of the rotor wake, the vertical velocity increases from a minimum value of about $15\ m/s$ in the proximity of the rotor disk to a maximum of approximately $19\ m/s$ at $z/R = -0.45$. The U_z velocity profiles for the upper ($h/R = 0.465$) and lower ($h/R = 0.681$) wing configurations show a similar behavior at a different vertical distance from the rotor disk due to the influence of the tilted wing. In particular, when the rotor wake flow is approaching the wing's leading edge, the vertical velocity slightly decreases. Therefore, an increase in the vertical velocity is observed for a vertical position below the wing leading edge, as the flow accelerates due to the local airfoil curvature. As shown in Fig. 20(d), for the upper wing configuration $h/R = 0.465$, the maximum vertical velocity reaches a value similar to the isolated rotor case. The CFD velocity profiles show a behavior similar to the measured profiles, in particular at $z/R = -0.30$ and -0.45. A larger discrepancy is visible at $z/R = -0.10$ and -0.20 closer to the blade and therefore to the vortex origin. In this region, the vortices are more concentrated and can induce higher velocities. Therefore, even a small discrepancy between the computed and measured vortex position will produce differences between the velocity profiles.

The PIV measurements on the y–constant planes, carried out for the upper wing case $h/R = 0.465$ only, allow analysis of the flow impinging on the wing sections. Figure 21 shows the comparison between the global–averaged PIV data and the unsteady CFD simulation results. The CFD velocity fields were obtained by averaging the velocity fields extracted at the same blade azimuthal positions on the last rotor revolution. The velocity fields are illustrated by means of the in–plane streamlines. The streamline patterns show that the tilted wing section experiences a positive angle of attack induced by the contribution of the rotor wake swirl. The observed flow field confirms the considerations about the airloads measured on the half–span wing in this configuration (see Fig. 8(a)). The behavior of the velocity fields on both y–constant planes is well captured by the numerical simulation. Figures 21(e) and 21(f) shows the comparisons of the U_x and U_z mean velocity profiles extracted at $x/R = 0$. The U_x component (corresponding to the rotor wake tangential velocity component) is constant in the plane at $y/R = -0.69$, with a value of about $3\ m/s$. In the outer plane ($y/R = -0.79$) U_x varies from $1\ m/s$ to a peak of $3\ m/s$ at $z/R = -0.23$ (see Fig. 21(e)). The peaks of the measured mean U_z are $15\ m/s$ and $19\ m/s$ in the inner and outer measurement planes, respectively (see Fig. 21(f)). Using the mean values of the U_x and U_z measured at the leading edge region, the estimated induced local angle of attack is close to 11° in the inner plane and 9° in the outer plane. These values are compatible with the loads measured on the half–span wing for this test condition. The comparison of both the U_x and U_z mean velocity profiles shows a fairly good agreement between CFD simulation and the experiment.

Conclusions

The present work described the results of an experimental and numerical investigation of the wing–rotor aerodynamic interaction for a tiltwing aircraft in hover. The performance of this aircraft configuration and the flow between rotor and wing were studied using separate rotor and wing strain gauge balances and PIV flow field surveys. Moreover, the use of high–fidelity CFD calculations resulted in a more detailed and complete description of the flow structures related to this aerodynamic interaction and improved understanding of the experimental data. Indeed, the CFD results show a good agreement with the measurements for the evaluation of the aircraft performance and for the reproduction of the flow field below the rotor.

The following conclusions are drawn from the presented results.

1) The rotor airloads measurements show an increase of the rotor performance obtained by tilting the external wing.

2) The results did not highlight any remarkable difference of the half–span model performance between the two wing vertical positions for hovering flight. As consequence, the wing–rotor vertical distance can be adjusted for other goals.

3) Both measurements and CFD calculations exhibited the presence of a small upload force on the wing system for the tilted configuration at high C_T/σ. This effect is related to the actual tilted wing incidence affected by the rotor wake swirl as confirmed by PIV surveys.

4) The unsteady CFD calculation revealed that the airload distribution on the rotor disk remains almost axi–symmetric with just a small thrust loss observed on the outer portion of the blade when passing over the wing. This effect is due to the interaction between a blade and the tip vortical structure released by the preceding bade.

5) The PIV surveys together with the unsteady CFD analysis resulted in a detailed insight of the flow physics of the rotor wake interaction with the wing. In particular, an analysis of the flow field illustrated the extent of the rotor wake boundary as well as the evolution of the spatial displacement of the tip vortex influenced by the vortex pairing. Indeed, for the higher wing position, the interaction with the tilted wing influences the contraction of the rotor wake with respect to the isolated rotor case. The quantification of wake contraction size could be used in the aircraft design to make the tilting wing span match the actual wake size.

References

[1] Foster, M., "The Future Evolution of the Tiltrotor," AIAA/ICAS International Air and Symposium and Exposition: The Next 100 Years of Flight, Dayton, OH, USA, July 14–17, 2003.

[2] Maisel, M., Giulianetti, D., and Dugan, D., "The History of the XV–15 Tilt Rotor Research Aircraft: From Concept to Flight," Monographs in Aerospace History, 17 SP–2000–4517, NASA History Division, 2000.

[3] Gazdag, D. and Altonin, L., "Potential Use of Tiltrotor Aricraft in Canadian Aviation," Technical Report TM–102245, NASA Technical Memorandum, 1990.

[4] Reber, R., "Civil TiltRotor Transportation for the 21^{st} Century," AIAA–93–4875, Presented at the AIAA International Powered Lift Conference, Santa Clara, CA, USA, December 1–3 1993.

[5] McVeigh, M., Grauer, W., and Paisley, D., "Rotor/Airframe Interaction On Tiltrotor Aircraft," *Journal of American Helicopter Society*, Vol. 35, (3), July 1990, pp. 43–51.

[6] Polak, D., Rehm, W., and George, A., "Effects of an Image Plane on the Tiltrotor Fountain Flow," *Journal of American Helicopter Society*, Vol. 45, (2), April 2000, pp. 90–96.

[7] Leishman, J. G. and Rosen, K. M., "Challenges in the Aerodynamic Optimization of High-Efficiency Proprotors," *Journal of the American Helicopter Society*, Vol. 56:012004, (1), January 2011, pp. 1–21.

[8] Darabi, A., Stalker, A., McVeigh, M., and Wygnanski, I., "The Rotor Wake Above a Tiltrotor Airplane–Model in Hover," 33^{rd} AIAA Fluid Dynamics Conference, Orlando, FL, USA, June 23–26, 2003.

[9]Felker, F. and Light, J. S., “Aerodynamic Interactions Between a Rotor and Wing in Hover,” *Journal of the American Helicopter Society*, Vol. 33, (2), April 1988, pp. 53–61.

[10]Potsdam, M. and Strawn, R., “CFD Simulations of Tiltrotor Configurations in Hover,” *Journal of the American Helicopter Society*, Vol. 50, (1), 2005, pp. 82–94.

[11]McVeigh, M. A., “The V–22 Tiltrotor Large–Scale Rotor Performance/Wing Download Test and Comparison With Theory,” *Vertica*, Vol. 10, (3/4), 1986, pp. 281–297.

[12]Felker, F., “Wing Download Results from a Test of a 0.658-Scale V–22 Rotor and Wing,” *Journal of the American Helicopter Society*, Vol. 37, (4), October 1992, pp. 58–63.

[13]McCluer, M. and Johnson, J., “Full–Span Tiltrotor Aeroacoustic Model (FS TRAM). Overview and Initial Testing,” American Helicopter Society Aerodynamics, Acoustics, and Test and Evaluation Technical Specialists’ Meeting, San Francisco, CA, USA, January 23–25, 2002.

[14]Young, L. A., E. R. Booth, J., Yamauchi, G. K., and Botha, G., “Overview of the Testing of a Small-Scale Proprotor,” American Helicopter Society 55^{th} Annual Forum, Montréal, Canada, May 25–27, 1999.

[15]Johnson, W., “Calculation of Tilt Rotor Aeroacoustic Model (TRAM DNW) Performance, Airloads, and Structural Loads,” American Helicopter Society Aeromechanics Specialists’ Meeting, Atlanta, GA, USA, November 2000.

[16]Young, L., Lillie, D., McCluer, M., Yamauchi, G., and Derby, M., “Insights into Airframe Aerodynamics and Rotor-on-Wing Interactions from a 0.25–Scale Tiltrotor Wind Tunnel Model,” American Helicopter Society Aerodynamics, Acoustics, and Test and Evaluation Technical Specialists’ Meeting, San Francisco, CA, USA, January 23–25, 2002.

[17]Wood, T. L. and Peryea, M. A., “Reduction of Tiltrotor Download,” *Journal of the American Helicopter Society*, Vol. 40, (3), July 1995, pp. 42–51.

[18]Nannoni, F., Giancamilli, G., and Cicalè, M., “Erica: the European Advance Tilt–Rotor,” 27^{th} European Rotorcraft Forum, Moscow, Russia, September 11–14, 2001.

[19]Gupta, V. and Baeder, J. D., “Investigation of Quad Tiltrotor Aerodynamics in Forward Flight Using CFD,” 20^{th} AIAA Applied Aerodynamics Conference, St. Louis, MO, USA, June 24–26, 2002.

[20]Lefebvre, T., Beaumier, P., Canard-Caruana, S., Pisoni, A., Pagano, A., Sorrentino, A., Van der Wall, B., Yin, J., Arzoumanian, C., Voutsinas, S., and Hermans, C., “Aerodynamic and Aero–Acoustic

Optimization of Modern Tilt–Rotor Blades Within the ADYN Project," 4^{th} European Congress on Computational Methods in Applied Sciences and Engineering, Jyväskylä, Finland, July 24–28, 2004.

[21] Decours, J., Burguburu, S., and Falissard, F., "Performance Assessment of the Erica Tilt-Rotor in Cruise," 36^{th} European Rotorcraft Forum, Paris, France, September 7–9, 2010.

[22] Dancik, P., Mazzitelli, F., and Peck, W., "Test Experience on the Vertol 76 VTOL Research Aircraft," American Helicopter Society 14^{th} Annual Forum, Washington, D.C., USA, April 16–19, 1958.

[23] Pegg, R., "Summary of Flight Test Results of the VZ–2 Tilt Wing Aircraft," NASA Technical Report TN D–989, February 1962.

[24] Markman, S. and Holder, W. G., *Straight Up: A History of Vertical Flight*, Schiffer Publications, 2000.

[25] Phillips, F., "The Canadair CL–84 Tilt-Wing V/STOL Programme," *The Aeronautical Journal*, Vol. 73, (704), August 1969.

[26] Alli, P., Nannoni, F., and Cicalè, M., "ERICA: The European Tiltrotor Design and Critical Technology Projects," AIAA/ICAS International Air and Space Symposium and Exposition: The Next 100 Years, Dayton, OH, USA, July 14–17, 2005.

[27] Hakkaart, J., Stabellini, A., Verna, A., de Bruin, A., Langer, H.-J., Schneider, O., Przybilla, M., Philipsen, I., Ragazzi, A., and Hoejmakers, A. H. W., "First NICETRIP Powered Wind Tunnel Tests Successfully Completed in DNW-LLF," American Helicopter Society 70^{th} Annual Forum, Montréal, Canada, May 20–22, 2014.

[28] Droandi, G., Gibertini, G., Lanz, M., Campanardi, G., Grassi, D., and Garbaccio, S., "Wing–Rotor Interaction On A 1/4–Scale Tiltrotor Half–Model," 39^{th} European Rotorcraft Forum, Moscow, Russia, September 3–6, 2013.

[29] Droandi, G., *Wing–Rotor Aerodynamic Interaction in Tiltrotor Aircraft*, Ph.D. thesis, Politecnico di Milano, 2014.

[30] Gibertini, G., Auteri, F., Campanardi, G., Macchi, C., Zanotti, A., and Stabellini, A., "Wind Tunnel Tests of a Tilt–Rotor Aircraft," *The Aeronautical Journal*, Vol. 115, (1167), May 2011, pp. 315–322.

[31] Beaumier, P., Decours, J., and Lefebvre, T., "Aerodynamic and Aeroacoustic Design of Modern Tilt–

Rotors: the ONERA Experience," 26^{th} International Congress of the Aeronautical Sciences, Anchorage, AK, USA, September 14–19, 2008.

[32]Chiaramonte, J. Y., Favier, D., Maresca, C., and Benneceur, S., "Aerodynamic Interaction Study of the Propeller/Wing Under Different Flow Configurations," *Journal of Aircraft*, Vol. 33, (1), 1996, pp. 46–53.

[33]Grife, A., Darabi, A., and Wygnanski, I., "Download Reduction on a Three Dimensional V–22 Model Using Active Flow Control," AIAA–2002–3071, Presented at the 1^{st} AIAA Flow Control Conference, St. Louis, MO, USA, June 24–26, 2002.

[34]Meakin, R., "Unsteady Simulation of the Viscous Flow About a V–22 Rotor and Wing in Hover," AIAA–95–3463, AIAA Atmospheric Flight Mechanics Conference Proceedings, Baltimore, MD, USA, August 7–10, 1995.

[35]Wissink, A., Potsdam, M., Sankaran, V., Sitaraman, J., Yang, Z., and Mavriplis, D., "A Coupled Unstructured–Adaptive Cartesian CFD Approach for Hover Prediction," American Helicopter Society 66^{th} Annual Forum, Phoenix, AZ, USA, May 11–13, 2010.

[36]Droandi, G., Gibertini, G., and Biava, M., "Wing–Rotor Aerodynamic Interaction in Tiltrotor Aircraft," 38^{th} European Rotorcraft Forum, Amsterdam, The Netherlands, September 4–7, 2012.

[37]Roskam, J., *Aircraft Design*, Roskam Aviation and Engineering Corporation, 1985.

[38]Torenbeek, E., *Synthesis of Subsonic Airplane Design*, Delft University Press, 1976.

[39]Droandi, G. and Gibertini, G., "Aerodynamic Blade Design with Multi–Objective Optimization for a Tiltrotor Aircraft," *Aircraft Engineering and Aerospace Technology*, Vol. 87, (1), 2015, pp. 19–29.

[40]Abbott, I. and Doenhoff, A. V., *Theory of Wing Sections, Including a Summary of Airfoil Data*, McGraw–Hill Book Co., Inc. (Reprinted by Dover Publications, 1959), 1949.

[41]L.K. Loftin, J., "Theoretical and Experimental Data for a Number of NACA 6A–Series Airfoil Section," Technical Report TR–903 (Supersedes NACA TN–1368), NACA, 1948.

[42]Farrell, M. K., "Aerodynamic Design of the V-22 Osprey Proprotor," American Helicopter Society 45^{th} Annual Forum, Boston, MA, USA, May 22–24, 1989.

[43]Swanson, A. A. and Light, J. S., "Shadowgraph Flow Visualization of Isolated Tiltrotor and Ro-

tor/Wing Wakes," American Helicopter Society 48th Annual Forum, Washington, D.C., USA, June 3–5, 1992.

[44] Bianchi, E., Russo, A., Kiessling, F., Ferrer, R., Dieterich, O., Frisoni, M. ., Bakker, R., Riziotis, V., Petot, D., and Lanz, M., "Numerical Whirl–Flutter Investigation of the European Tiltrotor Concept: Current Status and Future Prospects," 30th European Rotorcraft Forum, Marseilles, France, September 14–16, 2004.

[45] Droandi, G., Gibertini, G., Campanardi, G., Grassi, D., Macchi, C., and Peveroni, L., "Wind–Tunnel Rotor Model for Hover and Forward Flight Tests," AIDAA XXII Conference, Naples, Italy, September 9–12, 2013.

[46] Polak, D. and George, A., "Flowfield and Acoustic Measurements from a Model Tiltrotor in Hover," *Journal of Aircraft*, Vol. 35, (6), 1998, pp. 921–929.

[47] Zanotti, A., Grassi, D., and Gibertini, G., "Experimental Investigation of a Trailing Edge L–shaped Tab on a Pitching Airfoil in Deep Dynamic Stall Conditions," *Proc of IMechE, Part G: Journal of Aerospace Engineering*, Vol. 228, (12), 2014, pp. 2371–2382.

[48] PIVTEC, "PIVview 2C version 3.0. User manual," www.pivtec.com, January 2009.

[49] Raffel, M., Willert, C., and Kompenhans, J., *Particle Image Velocimetry, a Practical Guide*, Springer, 1998.

[50] Biava, M., Pisoni, A., Saporiti, A., and Vigevano, L., "Efficient Rotor Aerodynamics Predictions with an Euler Method," 29th European Rotorcraft Forum, Friedrichshafen, Germany, September 16–18, 2003.

[51] Spalart, P. and Allmaras, S., "One Equation Model for Aerodynamic Flows," AIAA–92–0439, Presented at the 30th AIAA Aerospace Science Meeting & Exhibit, Reno, NV, USA, January 6–9, 1992.

[52] Roe, P. L., "Approximate Riemann Solvers, Parameter Vectors and Difference Schemes," *Journal of Computational Physics*, Vol. 43, 1981, pp. 357–372.

[53] Venkatakrishnan, V., "On the Accuracy of Limiters and Convergence to Steady State Solutions," AIAA–1993–880, Presneted at the 31st AIAA Aerospace Science Meeting & Exhibit, Reno, NV, USA, January 11–14, 1993.

[54] Jameson, A., "Time Dependent Calculations Using Multigrid with Applications to Unsteady Flows

past Airfoils and Wings," AIAA–91–1596, Presented at the 10^{th} AIAA Computational Fluid Dynamics Conference, Honolulu, HI, USA, June 24–26, 1991.

[55] Biava, M., *RANS computations of rotor/fuselage unsteady interactional aerodynamics*, Ph.D. thesis, Politecnico di Milano, 2007.

[56] Hirsch, C., *Numerical computation of internal and external flows*, John Wiley & Sons, 1988.

[57] Chesshire, G. and Henshaw, W. D., "Composite Overlapping Meshes for the Solution of Partial Differential Equations," *Journal of Computational Physics*, Vol. 90, 1990, pp. 1–64.

[58] Biava, M., Valentini, M., and Vigevano, L., "Trimmed Actuator Disk Modeling for Helicopter Rotor," 39^{th} European Rotorcraft Forum, Moscow, Russia, September 3–6, 2013.

[59] Turkel, E., Radespiel, R., and Kroll, N., "Assessment of Preconditioning Methods for Multidimensional Aerodynamics," *Computer and Fluids*, Vol. 26, (6), 1997, pp. 613–634.

[60] Bhagwat, M. and Leishman, G., "On the Aerodynamic Stability of Helicopter Rotor Wakes," *AIAA Journal*, Vol. 38, (2), 2000, pp. 301–308.

[61] Metcalfe, R., Orszag, S., Brachet, M., Menon, S., and Riley, J., "Secondary instability of a temporally growing mixing layer," *Journal of Fluid Mechanics*, Vol. 184, 1987, pp. 207–243.

[62] Gibertini, G., Mencarelli, A., and Zanotti, A., "Oscillating Aerofoil and Perpendicular Vortex Interaction," *Proc of IMechE, Part G: Journal of Aerospace Engineering*, Vol. 228, (6), 2014, pp. 846–858.

Passengers	20 + baggage
Crew	2 pilots
Maximum cruise speed	170 m/s
Rotor speed (Helicopter)	560 rpm
Rotor speed (Airplane)	430 rpm
Empty weight	7100 kg
Gross weight	11600 kg
Wing span	15.0 m
Wing root chord	3.0 m
Wing tilt section chord	2.5 m
Wing tip chord	2.0 m
Fixed wing span	3.732 m
Wing airfoil	NACA 64A221
Number of blades	4
Rotor radius	3.7 m
Wing–rotor distance (h/R)	0.465

Table 1. Reference full–scale aircraft details.

Trim condition	C_T/σ	θ [deg]
TC1	0.007	2
TC2	0.021	4
TC3	0.035	6
TC4	0.047	8
TC5	0.064	10
TC6	0.078	12
TC7	0.094	14

Table 2. Rotor Trim Conditions for steady calculations. Data taken from steady isolated rotor simulations in hover (see [29]).

	Steady case		Unsteady case	
Grids	No. Blocks	No. Cells ($\times 10^6$)	No. Blocks	No. Cells ($\times 10^6$)
Far–field 1	5	0.629	5	0.629
Far–field 2	6	1.451	6	1.451
Nacelle	6	2.803	6	2.803
Nacelle inter.	4	3.113	4	3.113
Wing 1	6	1.816	6	1.816
Wing 2	9	2.185	9	2.185
Actuator Disk	1	0.290		
Blade			8 ($\times 4$)	1.813 ($\times 4$)
Total	37	12.287	68	19.249

Table 3. Computational grid details for half–aircraft steady/unsteady calculations.

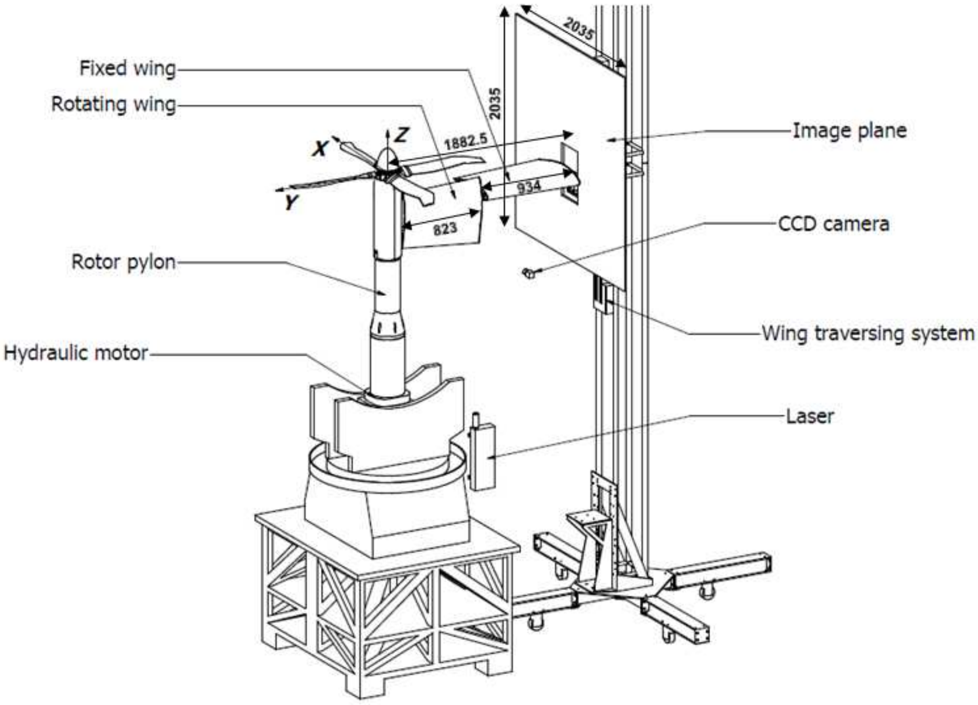

Fig. 1 Schematic view of the experimental test rig and coordinate axis of the x–y–z reference system. PIV set up included.

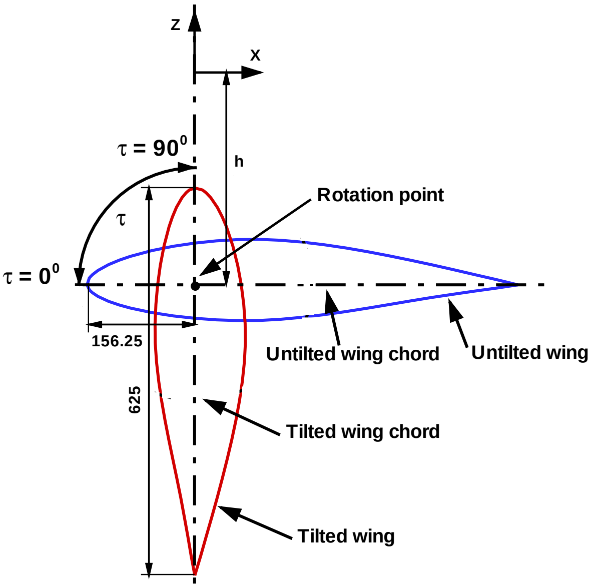

Fig. 2 Schematic view of the wing layout, dimensions in mm.

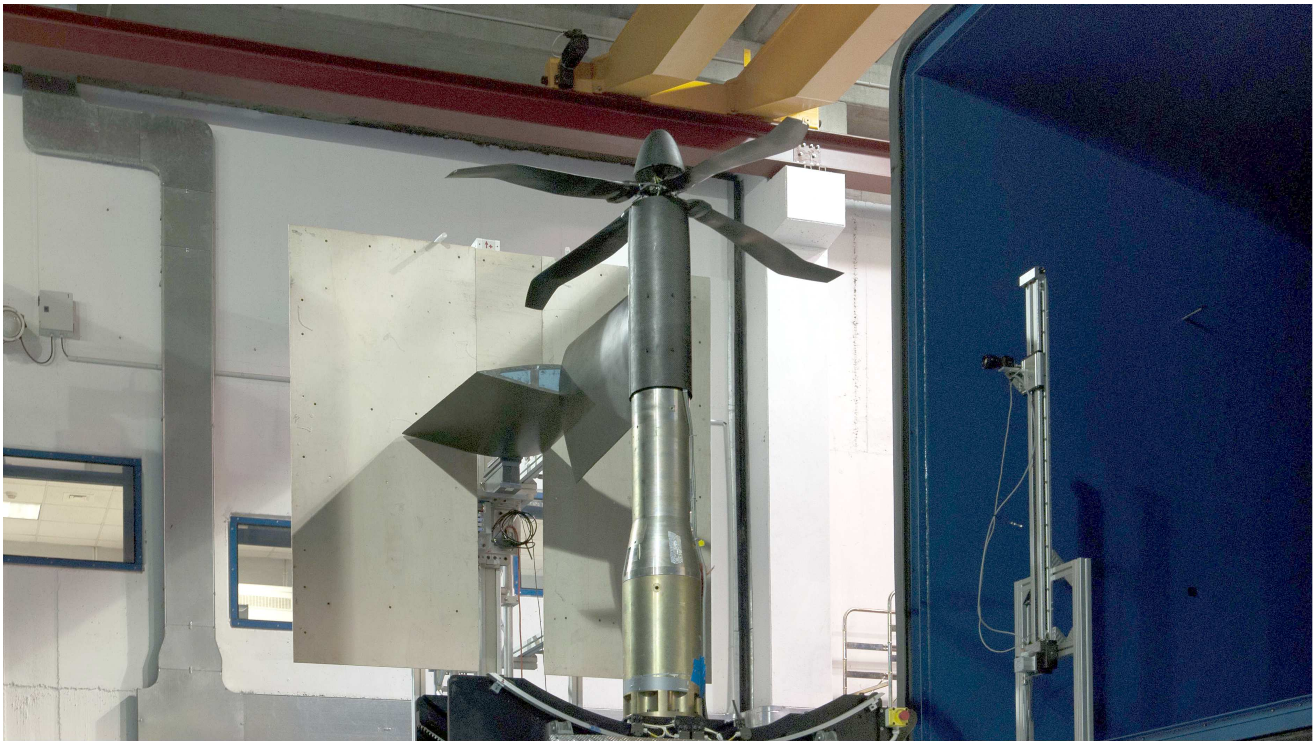

Fig. 3 The half–model test rig in the open test section of the Politecnico di Milano GVPM.

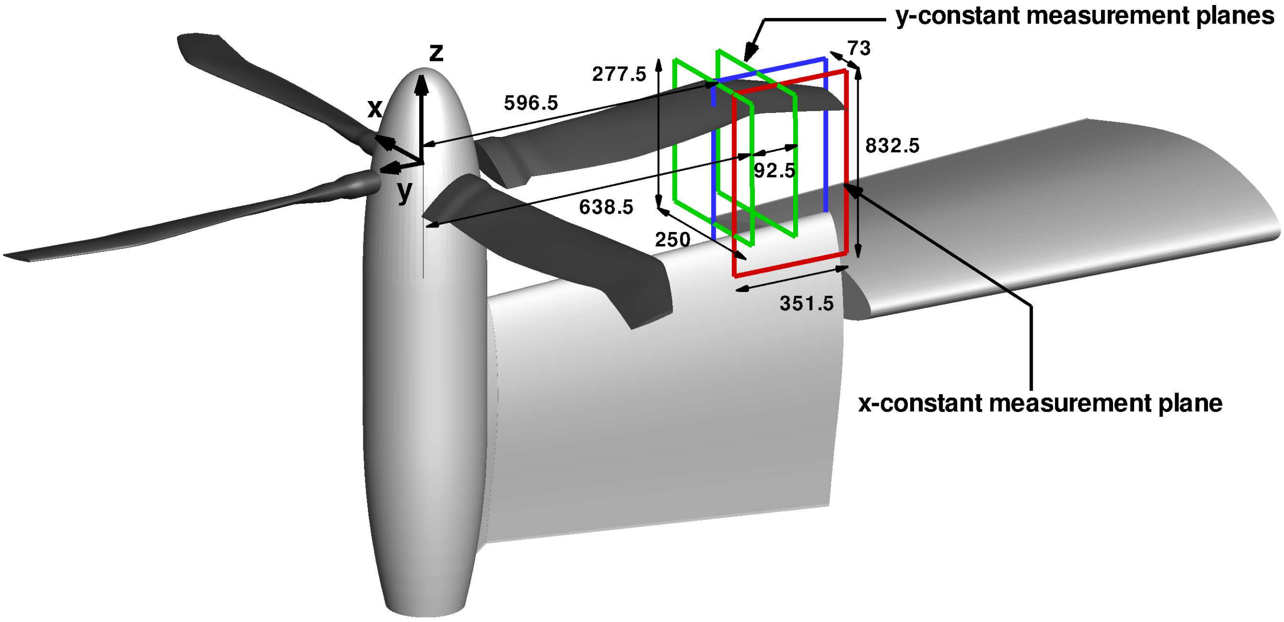

Fig. 4 Schematic view of the PIV planes, dimensions in mm.

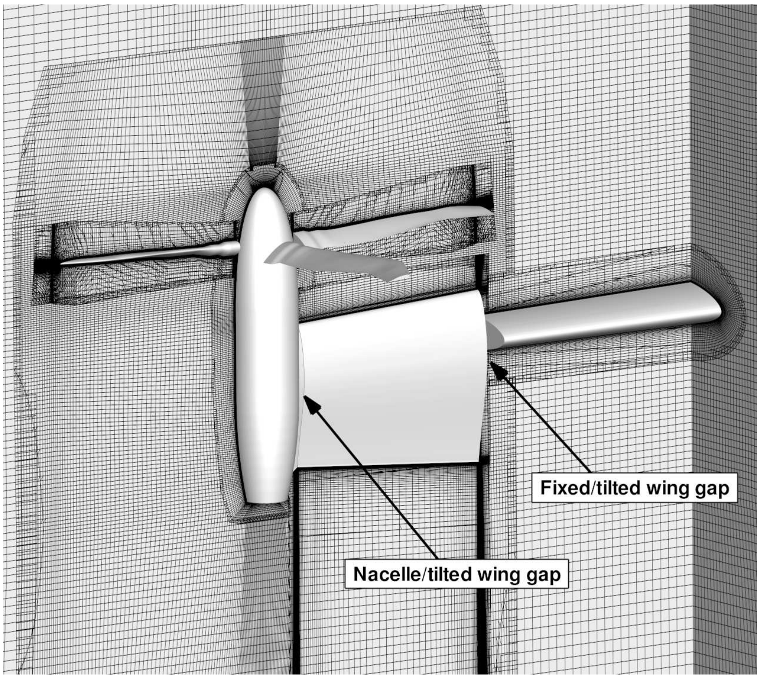

(a) Frontal view

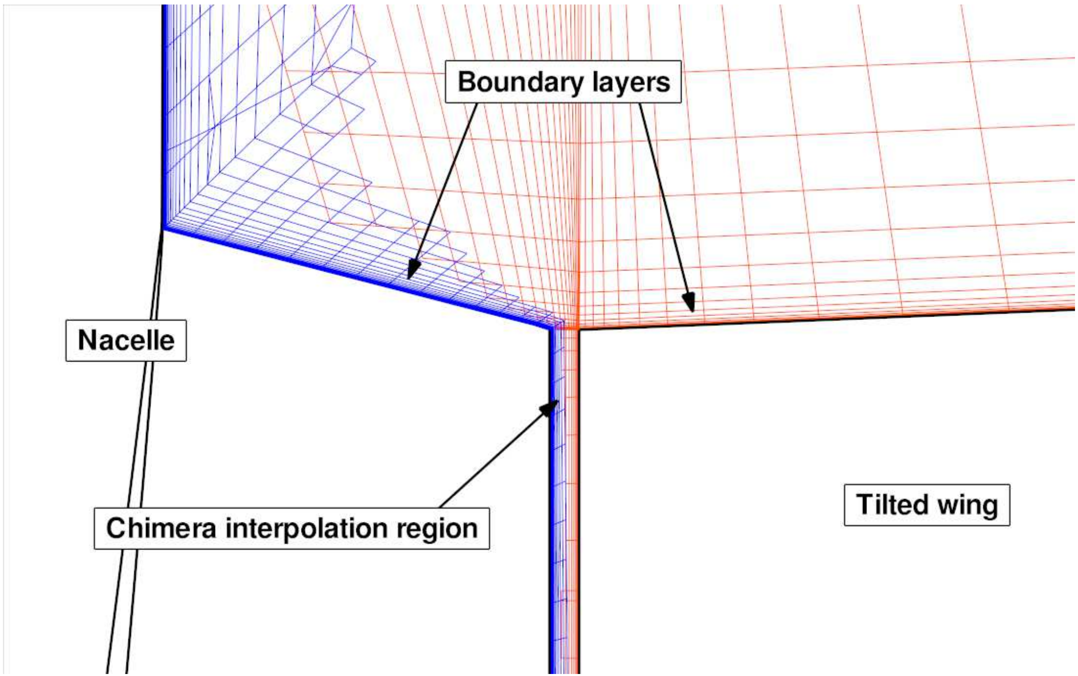

(b) Outer wing/nacelle gap detail

Fig. 5 Details of grids system for CFD calculations.

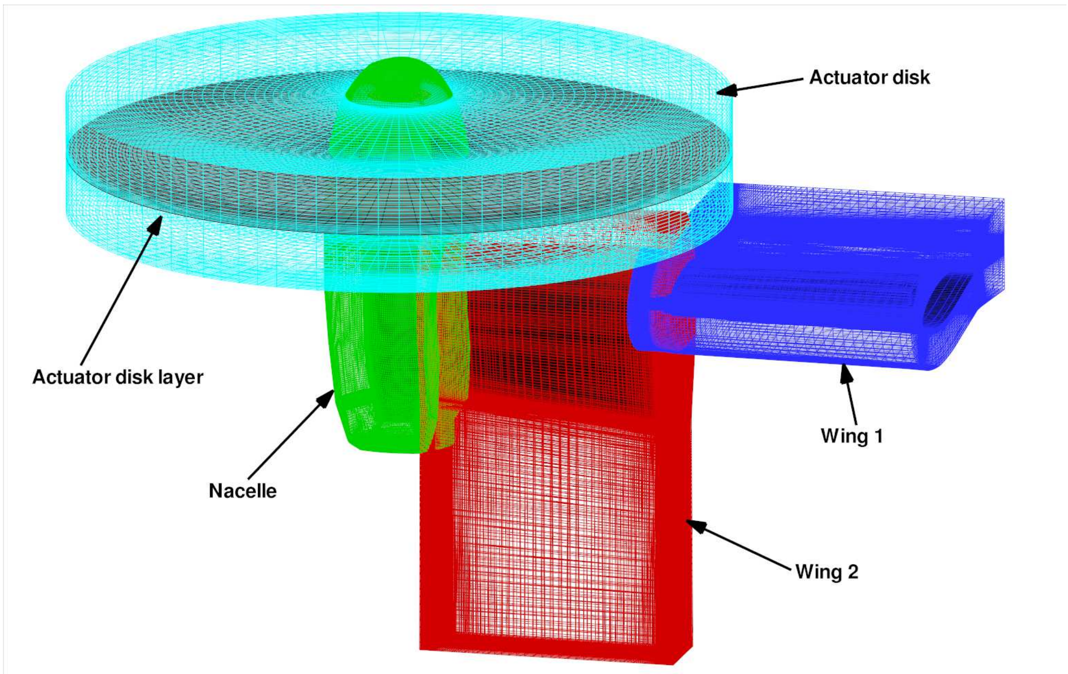

(a) Steady case

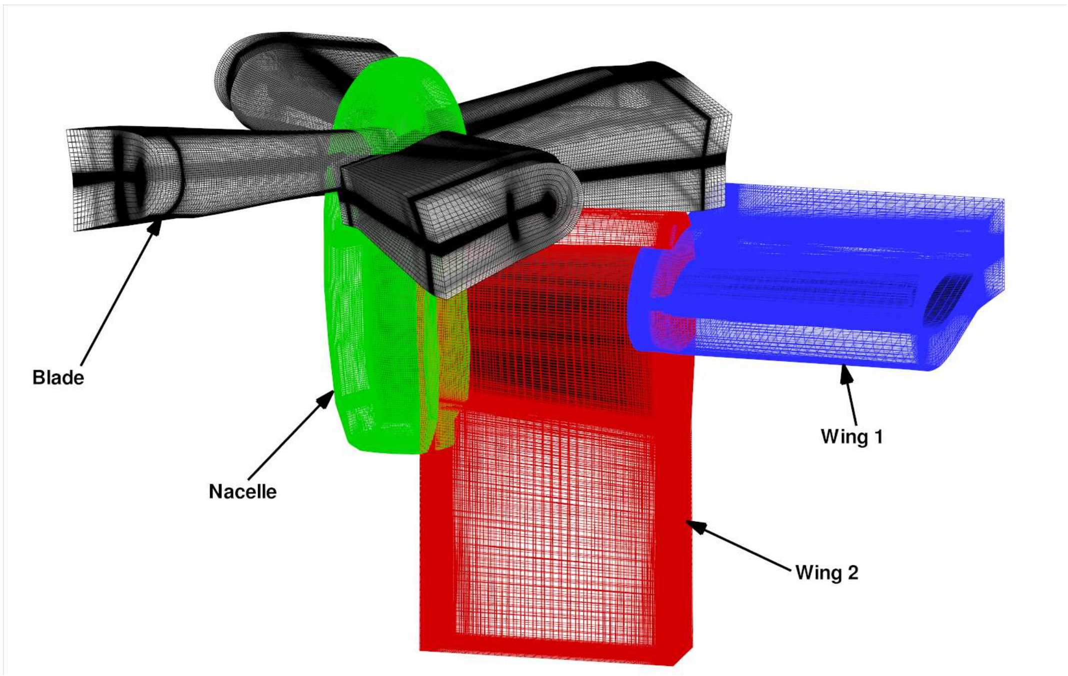

(b) Unsteady case

Fig. 6 View of grids system for CFD calculations.

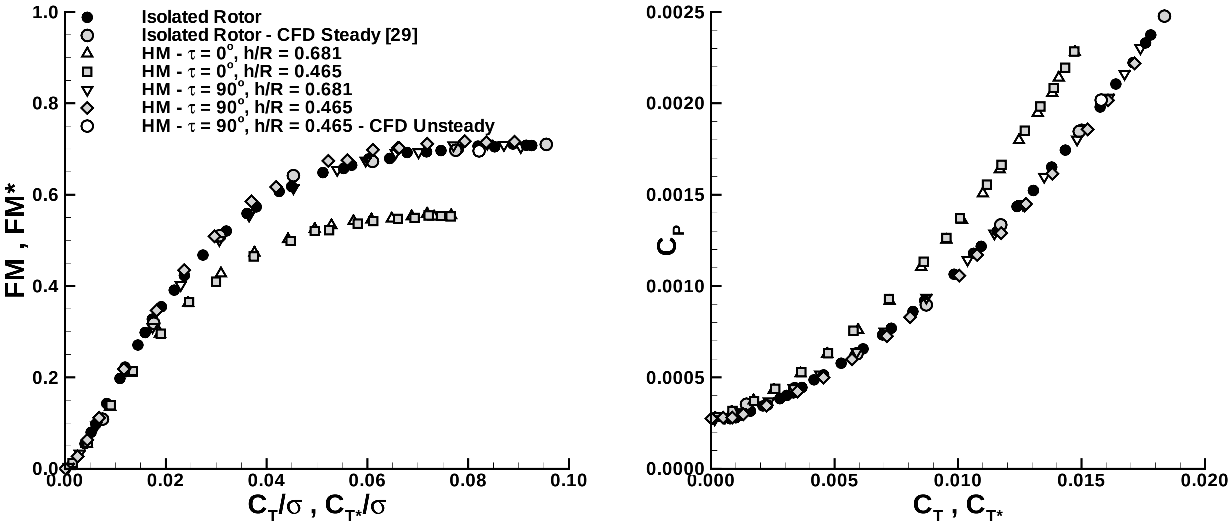

(a) (b)

Fig. 7 Influence of configurations on rotor performance in hover: a) FM as function of C_T/σ, b) C_P as function of C_T, for $M_{tip} = 0.32$.

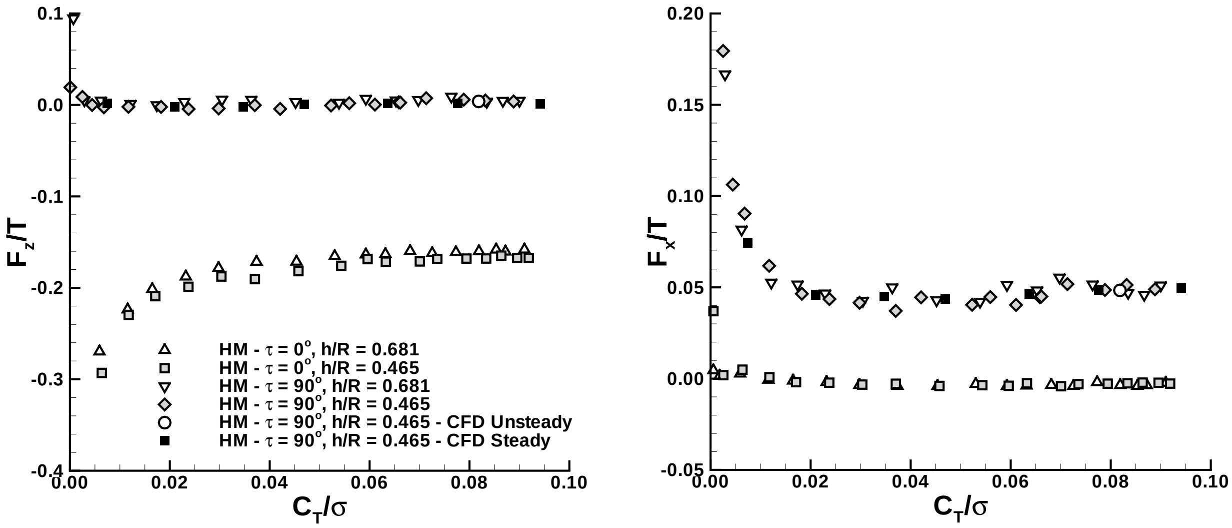

(a) (b)

Fig. 8 Influence of configurations on wing loads in hover: a) F_z/T and b)F_x/T as function of C_T/σ, for $M_{tip} = 0.32$.

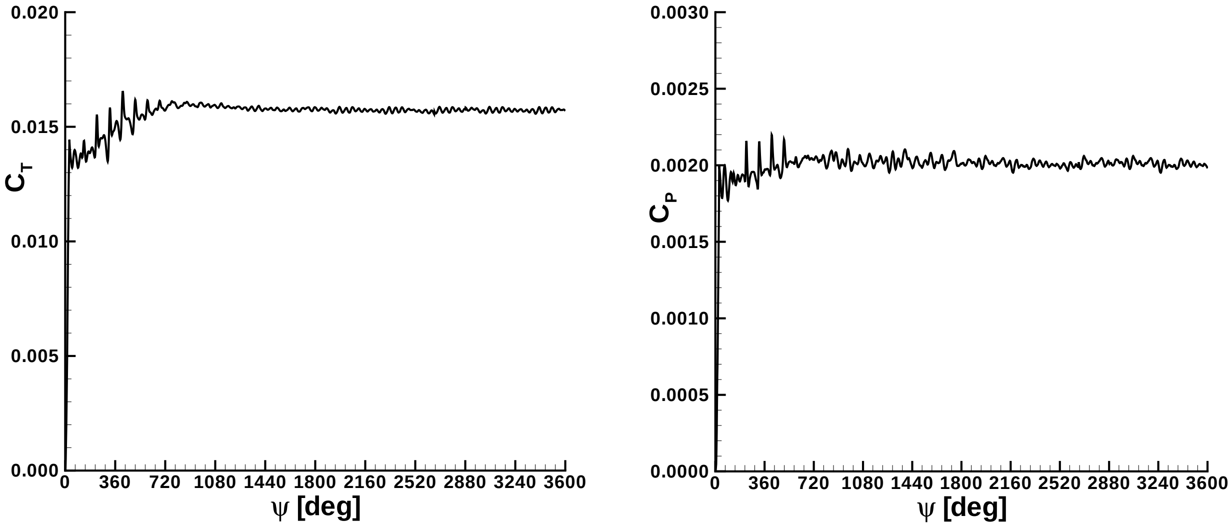

(a) (b)

Fig. 9 Rotor load time history from unsteady CFD calculation for $\tau = 90°$: a) rotor thrust T and b) rotor power P, TC6 ($\theta = 12°$, $\beta = 2.5°$, $M_{tip} = 0.32$).

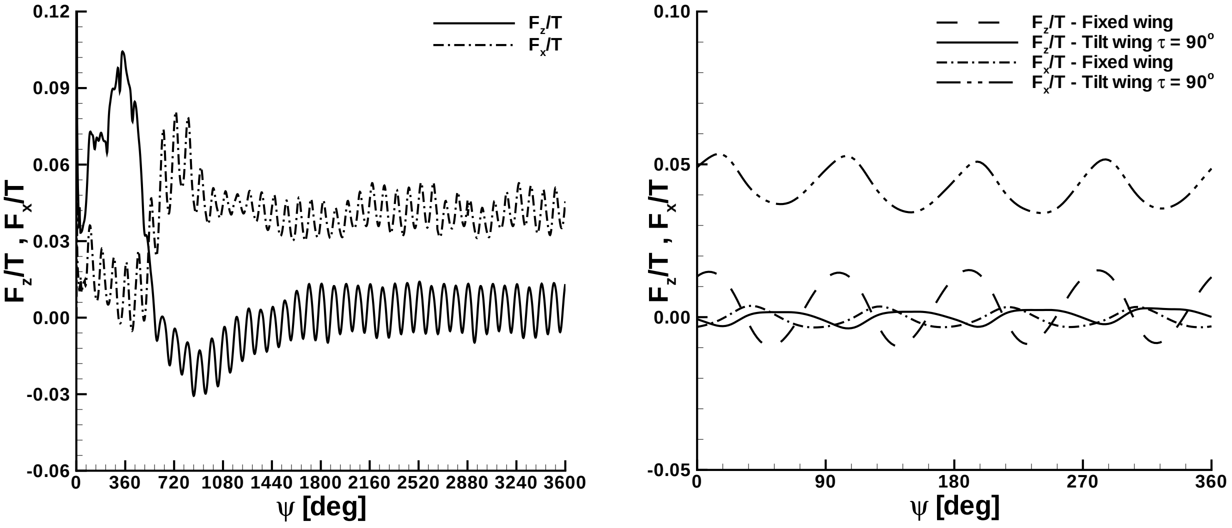

(a) (b)

Fig. 10 Wing load time history from unsteady CFD calculation for $\tau = 90°$: a) wing global F_x and F_z and b) detail on last rotor revolution, TC6 ($\theta = 12°$, $\beta = 2.5°$, $M_{tip} = 0.32$).

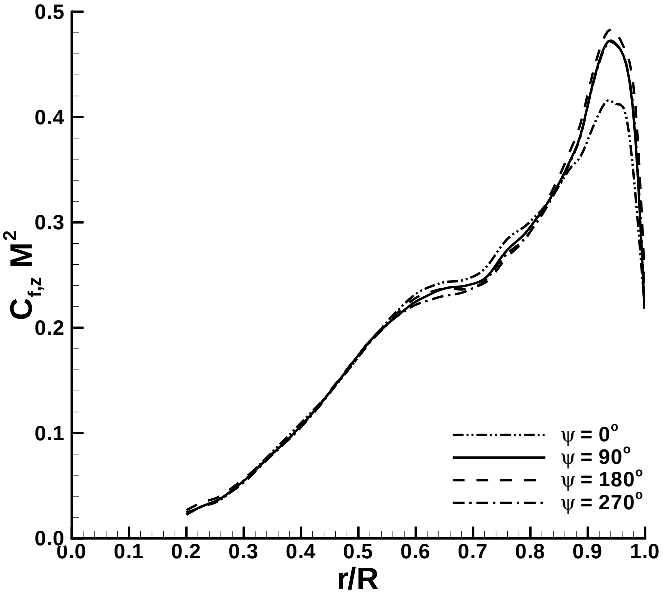

Fig. 11 Blade load distributions from unsteady CFD calculation for $\tau = 90°$, TC6 ($\theta = 12°$, $\beta = 2.5°$, $M_{tip} = 0.32$).

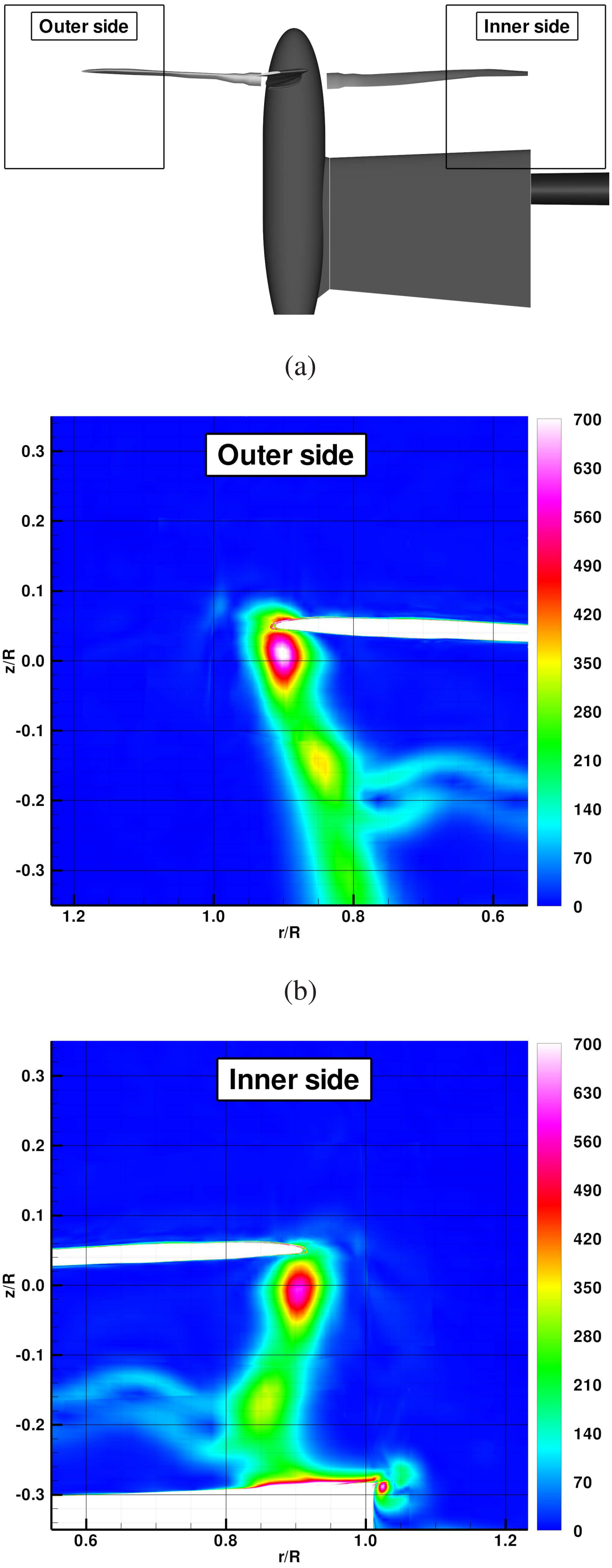

Fig. 12 Unsteady CFD results: vorticity magnitude $\|\Omega\|$ contours around the blade at $\psi = 0°$.

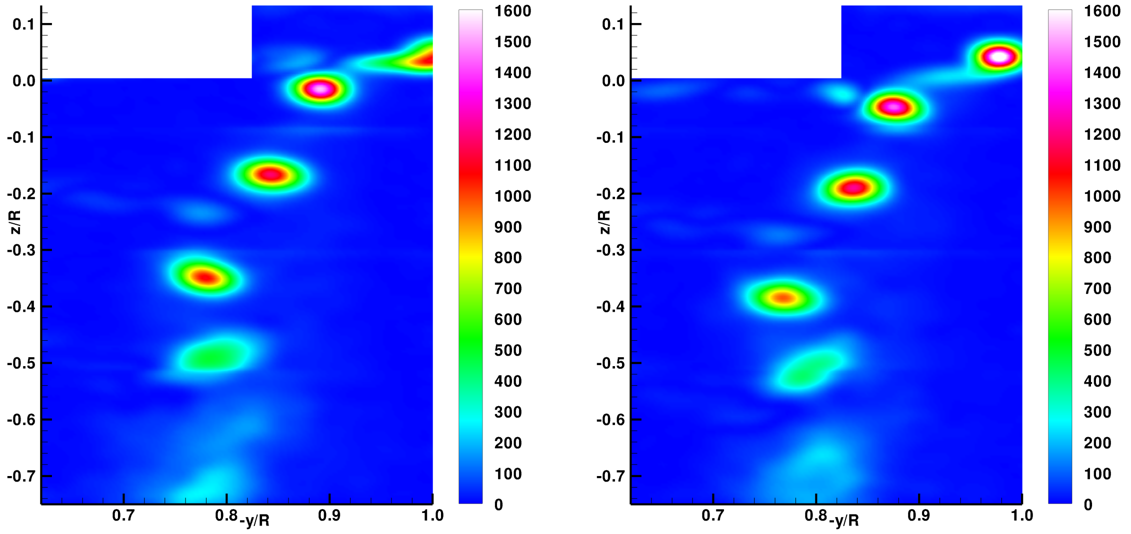

(a) $\psi = 15°$ (b) $\psi = 30°$

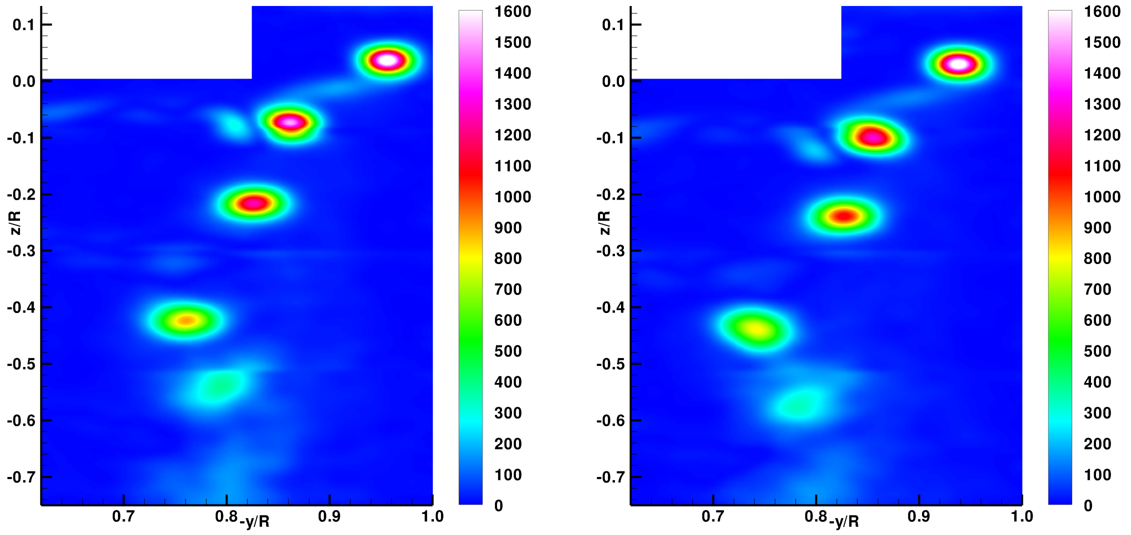

(c) $\psi = 45°$ (d) $\psi = 60°$

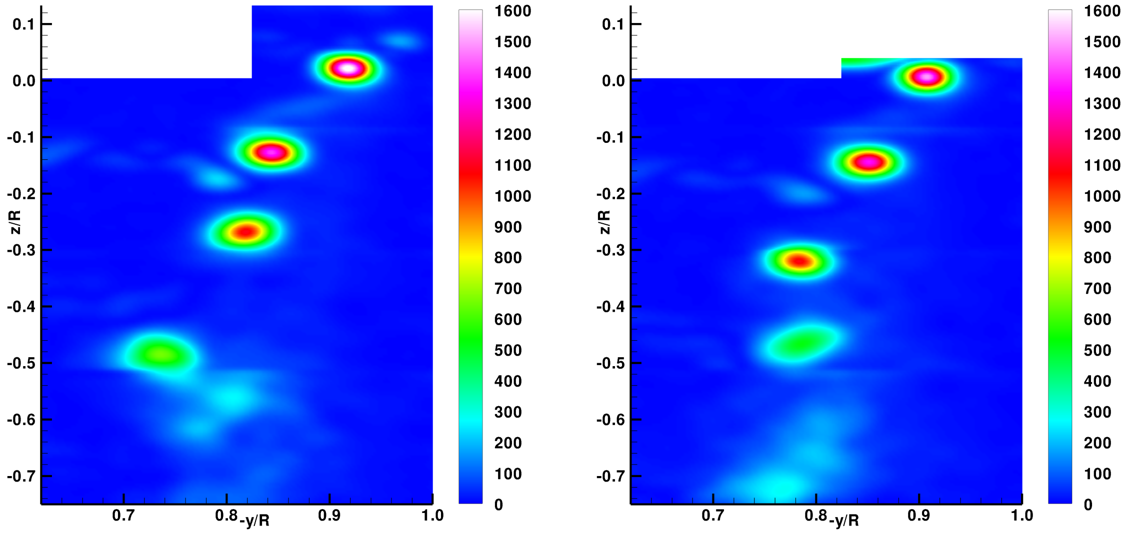

(e) $\psi = 75°$ (f) $\psi = 90°$

Fig. 13 PIV results for isolated rotor: phase–locked vorticity contours $[1/s]$, TC6 ($\theta = 12°$, $\beta = 2.5°$, $M_{tip} = 0.32$).

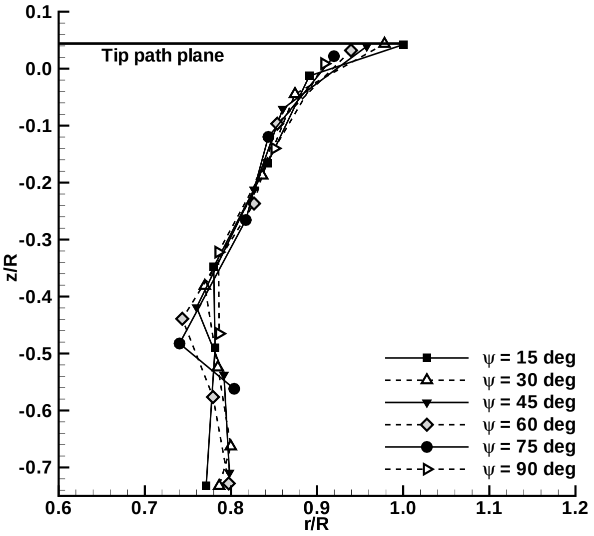

Fig. 14 Tip vortex core displacements in $r - z$ plane: isolated rotor wake boundaries at different blade azimuthal positions, TC6 ($\theta = 12°$, $\beta = 2.5°$, $M_{tip} = 0.32$).

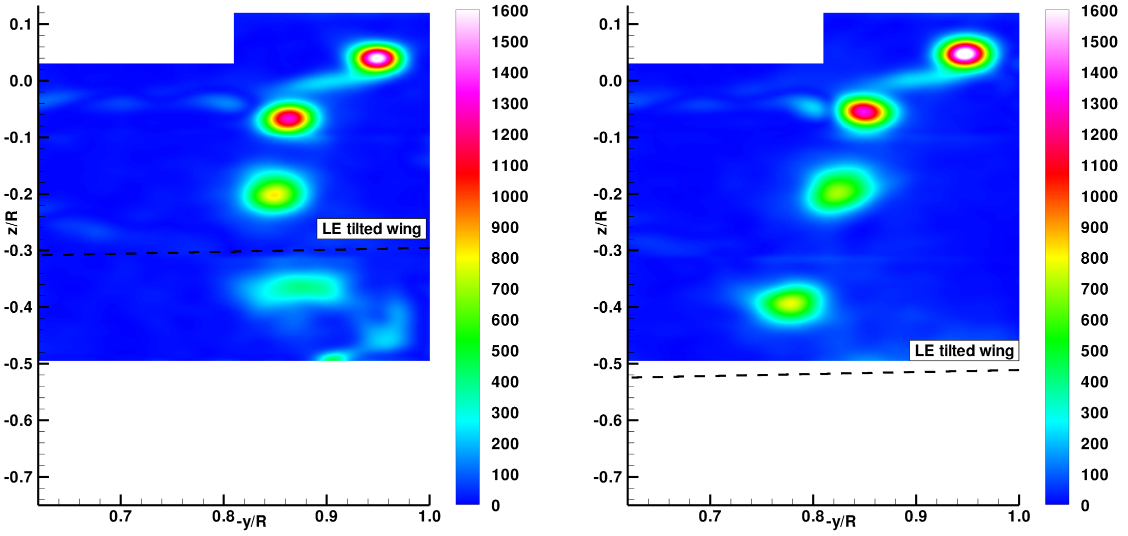

(a) $\psi = 30°$, $h/R = 0.465$ (b) $\psi = 30°$, $h/R = 0.681$

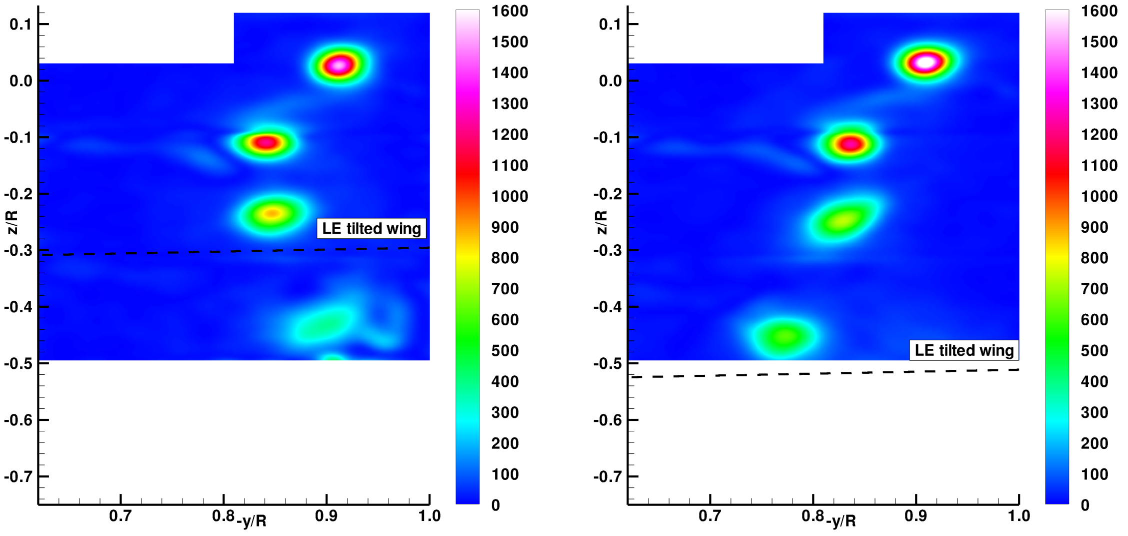

(c) $\psi = 60°$, $h/R = 0.465$ (d) $\psi = 60°$, $h/R = 0.681$

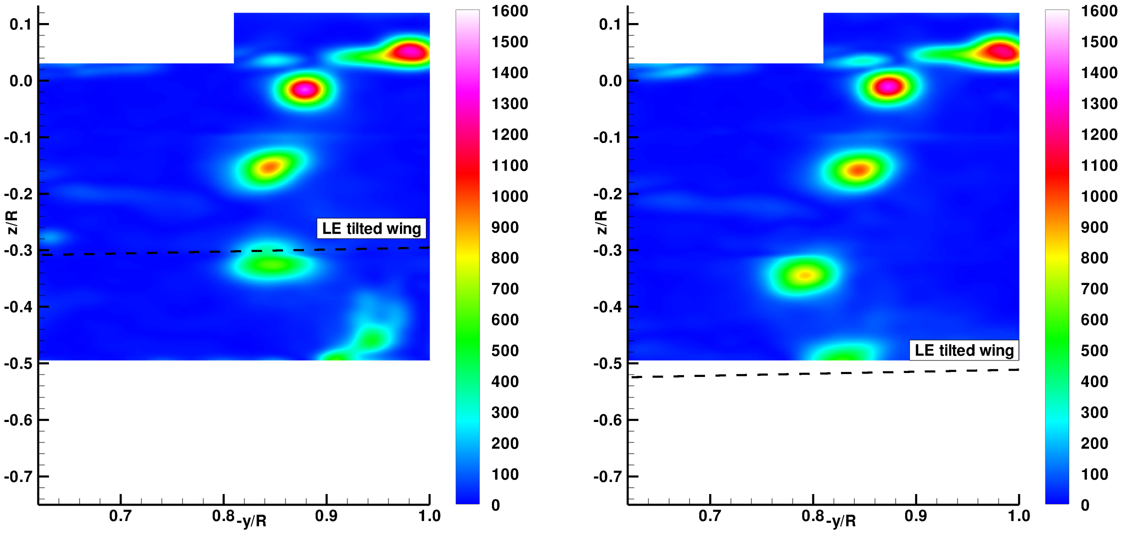

(e) $\psi = 90°$, $h/R = 0.465$ (f) $\psi = 90°$, $h/R = 0.681$

Fig. 15 PIV results for half–span model configuration, $\tau = 90°$: phase–locked vorticity contours $[1/s]$, TC6 ($\theta = 12°$, $\beta = 2.5°$, $M_{tip} = 0.32$).

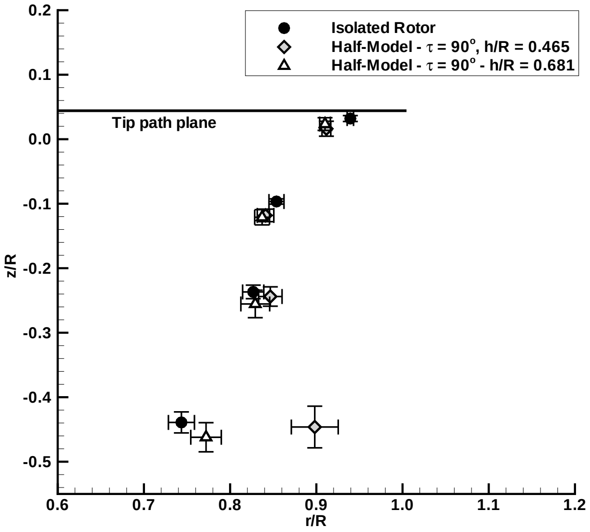

Fig. 16 Tip vortex center locations with the corresponding standard deviation (azimuthal blade position $\psi = 60°$): comparison between the isolated rotor and the half–model tilted wing configurations, TC6 ($\theta = 12°$, $\beta = 2.5°$, $M_{tip} = 0.32$).

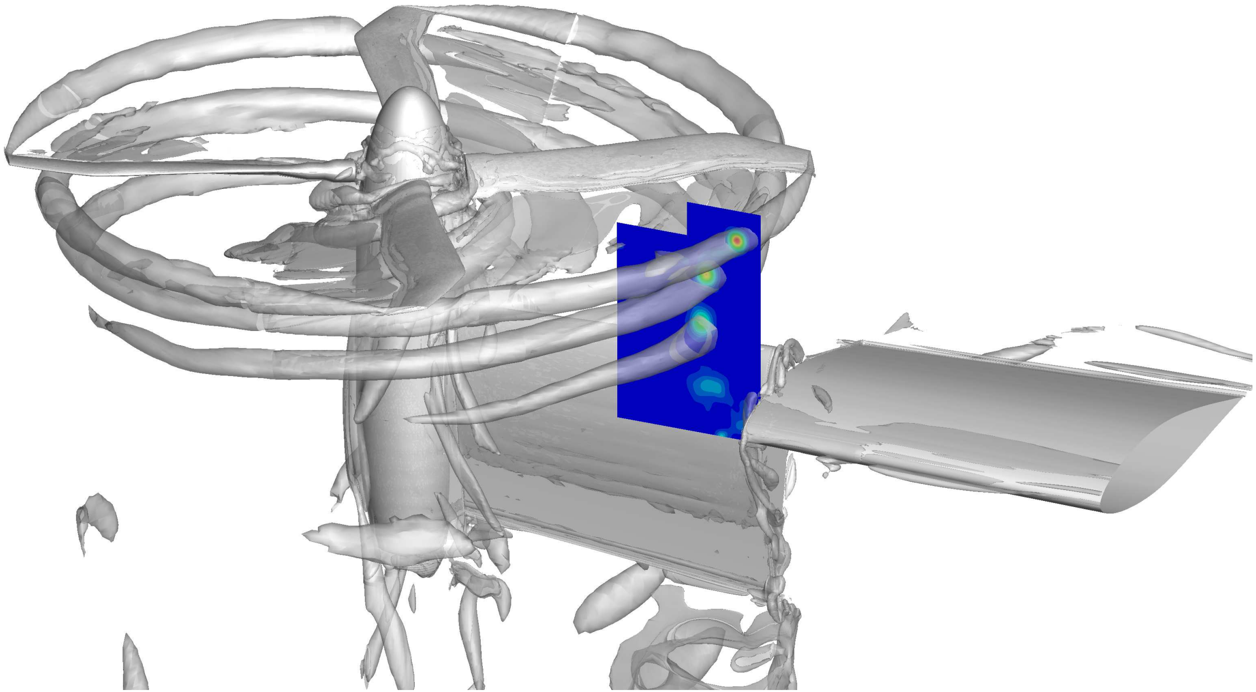

(a) $\psi = 30°$

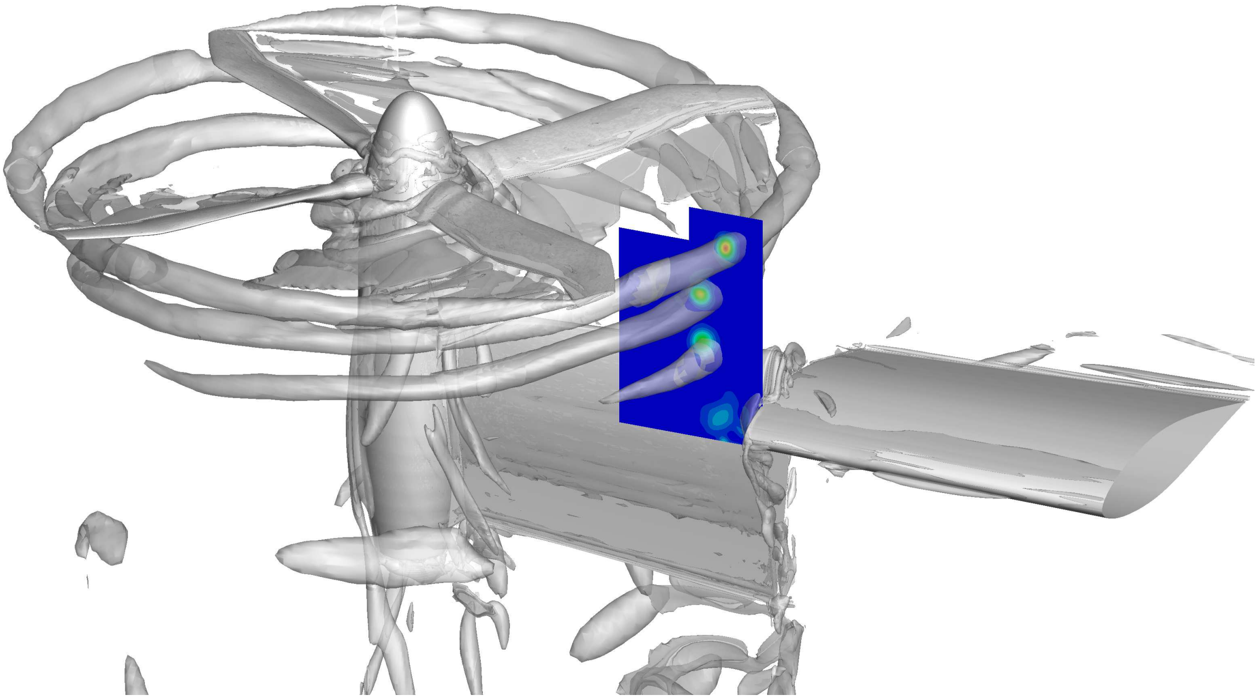

(b) $\psi = 60°$

Fig. 17 CFD visualization of the Q criteria wake iso–surfaces ($Q = 2.5 \times 10^{-2}$, non–dimensional) and comparison with vorticity in the x–constant PIV plane, $h/R = 0.465$, TC6 ($\theta = 12°$, $\beta = 2.5°$, $M_{tip} = 0.32$).

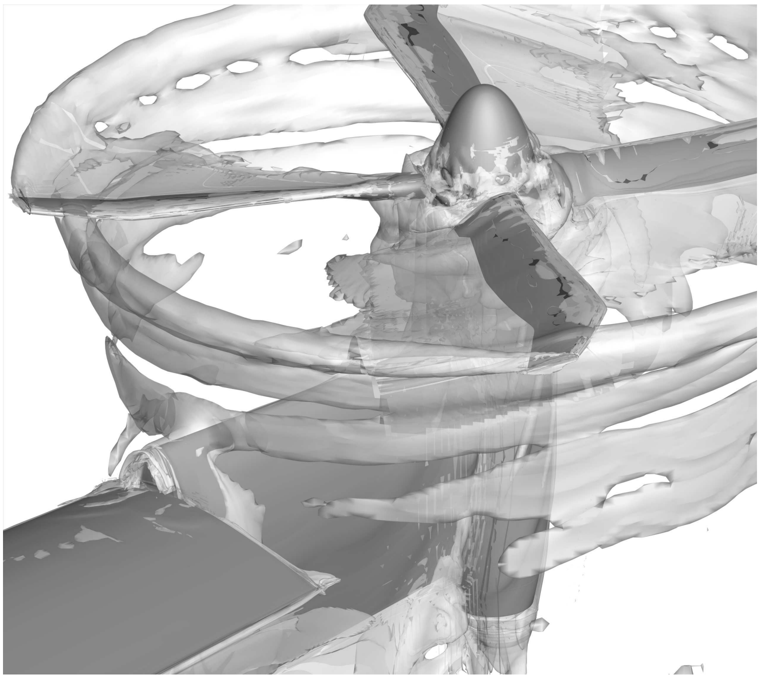

Fig. 18 CFD visualization of the vorticity magnitude iso–surfaces ($\|\mathbf{\Omega}\| = 210\ [1/s]$), $\tau = 90°$, $h/R = 0.465$, $\psi = 60°$, TC6 ($\theta = 12°$, $\beta = 2.5°$, $M_{tip} = 0.32$).

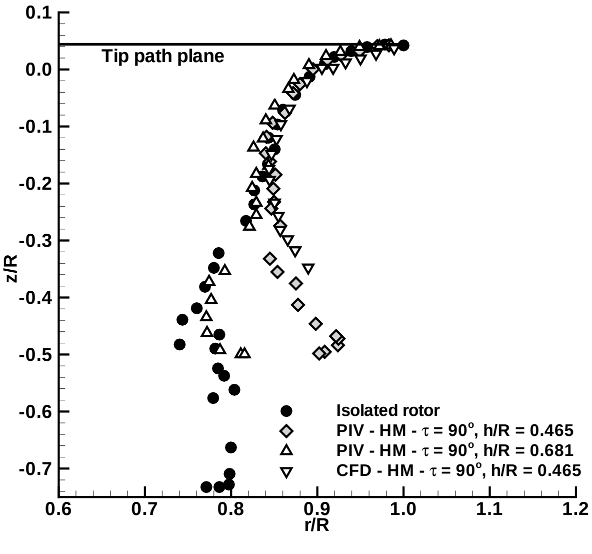

Fig. 19 Tip vortex core displacements: comparison between the isolated rotor and the half–model tilted wing configurations, TC6 ($\theta = 12°$, $\beta = 2.5°$, $M_{tip} = 0.32$).

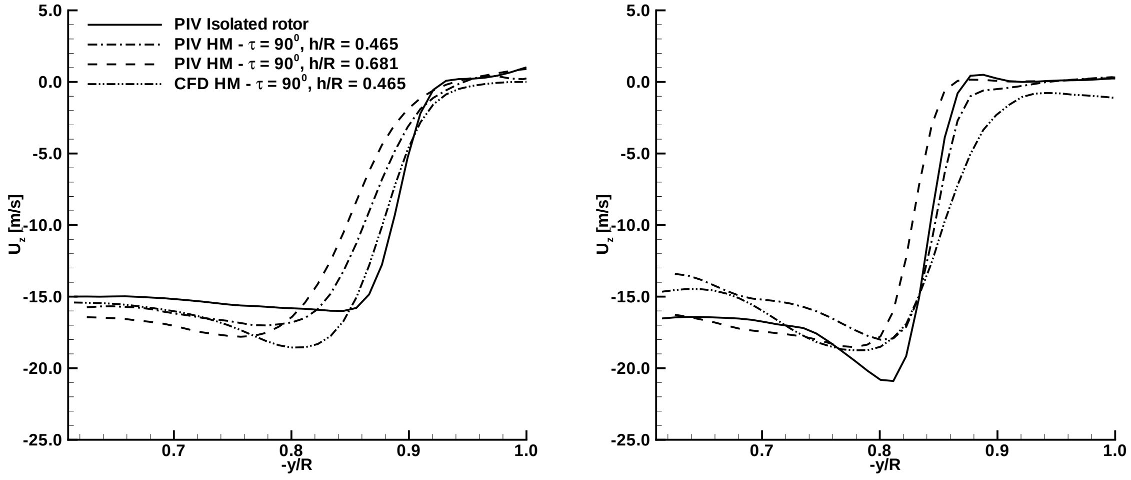

(a) $z/R = -0.10$ (b) $z/R = -0.20$

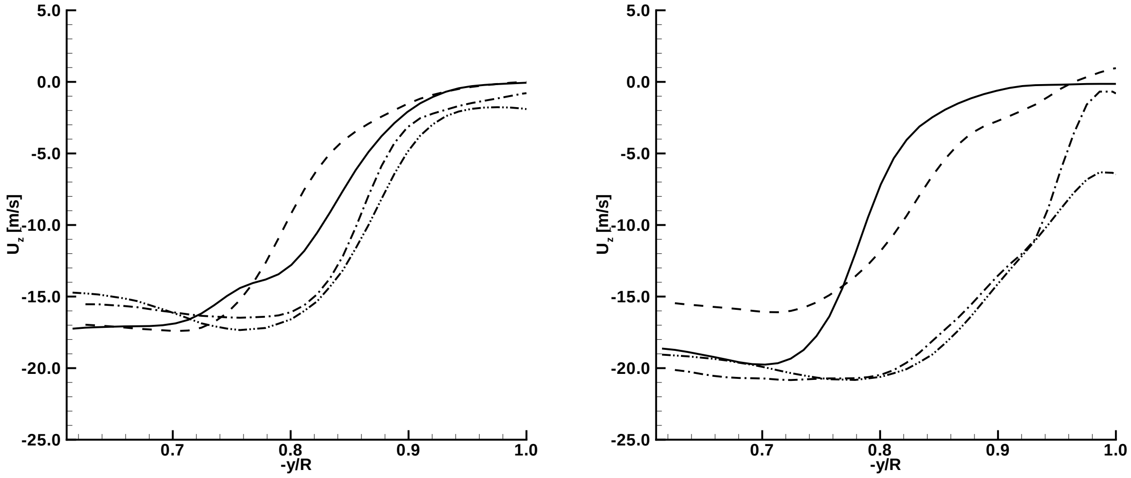

(c) $z/R = -0.30$ (d) $z/R = -0.45$

Fig. 20 Comparison between U_z velocity component profiles for Isolated rotor, Half–span model with wing at $h/R = 0.465$, $h/R = 0.681$ and CFD results at $\psi = 15°$, TC6 ($\theta = 12°$, $\beta = 2.5°$, $M_{tip} = 0.32$).

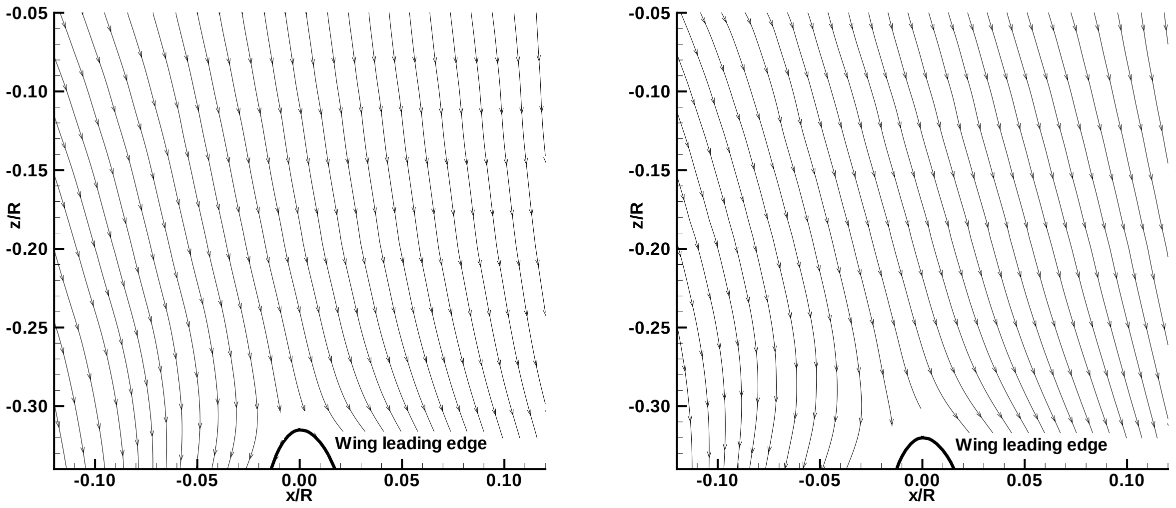

(a) $y/R = -0.79$, PIV (b) $y/R = -0.69$, PIV

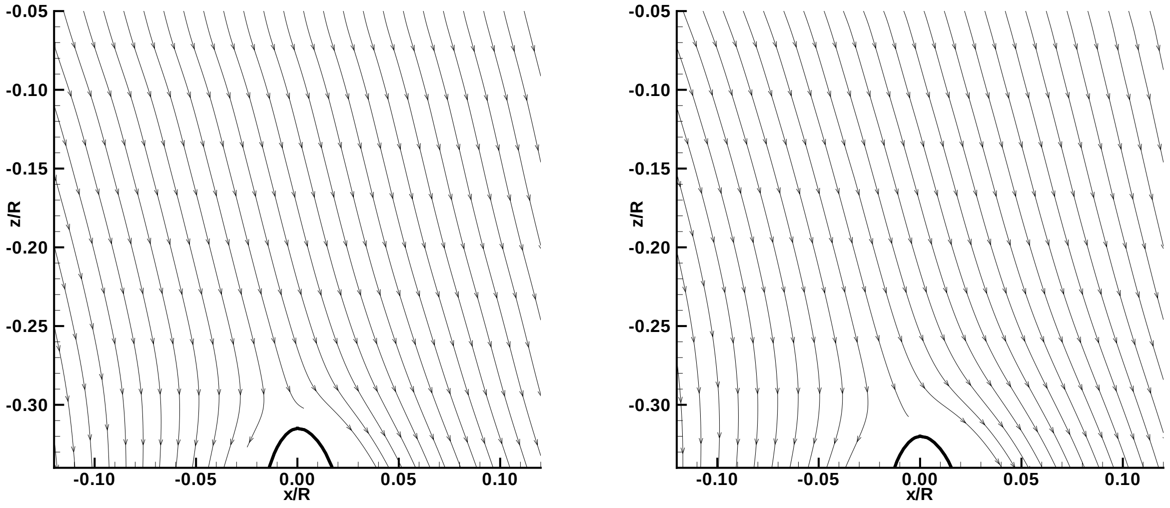

(c) $y/R = -0.79$, CFD (d) $y/R = -0.69$, CFD

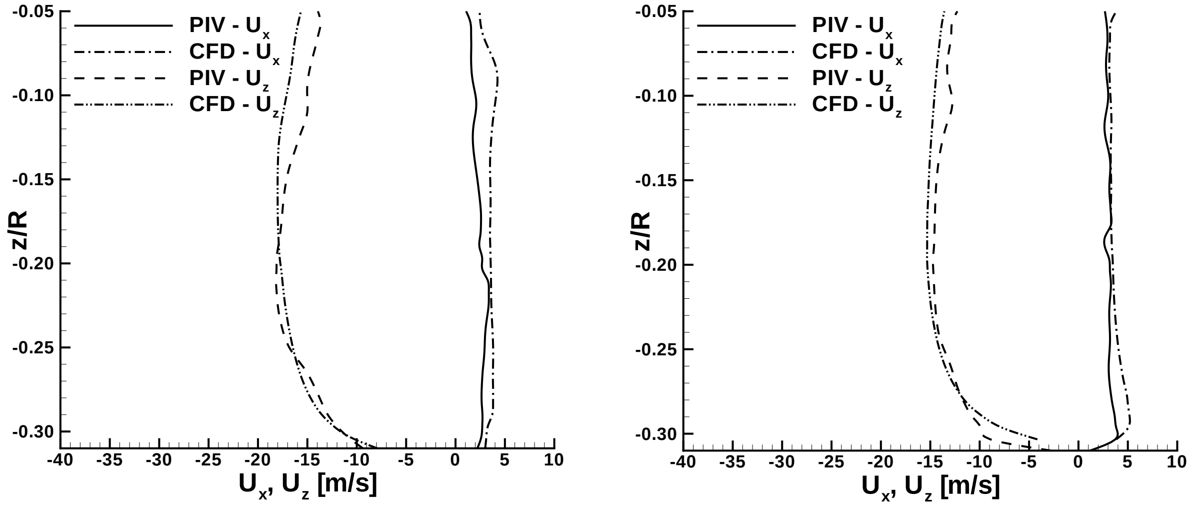

(e) $y/R = -0.79$ (f) $y/R = -0.69$

Fig. 21 Comparison between PIV and unsteady CFD on y–constant planes: a-d) in–plane streamlines, e-f) U_x and U_z mean velocity component profiles extracted in correspondence of the tilted wing leading edge, TC6 ($\theta = 12°$, $\beta = 2.5°$, $M_{tip} = 0.32$).